



**HAL**  
open science

## Role of thermodynamic and turbulence processes on the fog life cycle during SOFOF3D experiment

Cheikh Dione, Martial Haeffelin, Frédéric Burnet, Christine Lac, Guylaine Canut, Julien Delanoë, Jean-Charles Dupont, Susana Jorquera, Pauline Martinet, Jean-François Ribaud, et al.

### ► To cite this version:

Cheikh Dione, Martial Haeffelin, Frédéric Burnet, Christine Lac, Guylaine Canut, et al.. Role of thermodynamic and turbulence processes on the fog life cycle during SOFOF3D experiment. Atmospheric Chemistry and Physics Discussions, In press, 10.5194/egusphere-2023-1224 . hal-04126797v1

**HAL Id: hal-04126797**

**<https://hal.science/hal-04126797v1>**

Submitted on 13 Jun 2023 (v1), last revised 21 Dec 2023 (v2)

**HAL** is a multi-disciplinary open access archive for the deposit and dissemination of scientific research documents, whether they are published or not. The documents may come from teaching and research institutions in France or abroad, or from public or private research centers.

L'archive ouverte pluridisciplinaire **HAL**, est destinée au dépôt et à la diffusion de documents scientifiques de niveau recherche, publiés ou non, émanant des établissements d'enseignement et de recherche français ou étrangers, des laboratoires publics ou privés.



Distributed under a Creative Commons Attribution 4.0 International License



1     **Role of thermodynamic and turbulence processes on the fog life cycle during**  
2   **SOFOG3D experiment**

3     Cheikh DIONE<sup>1\*</sup>, Martial HAEFFELIN<sup>1</sup>, Frederic BURNET<sup>2</sup>, Christine LAC<sup>2</sup>, Guylaine CANUT<sup>2</sup>, Julien  
4     DELANOË<sup>3</sup>, Jean-Charles DUPONT<sup>4</sup>, Susana JORQUERA<sup>3</sup>, Pauline MARTINET<sup>2</sup>, Jean-Francois  
5     RIBAUD<sup>5</sup>, and Felipe TOLEDO<sup>3</sup>

6     1) Institut Pierre Simon Laplace, CNRS, Ecole Polytechnique de Paris, Institut Polytechnique de Paris, Paris, France

7     2) Météo-France, Toulouse, France

8     3) Laboratoire Atmosphères, Milieux, Observations Spatiales/UVSQ/CNRS/UPMC, 78280 Guyancourt, France

9     4) Institut Pierre-Simon Laplace, Ecole Polytechnique, UVSQ, Université Paris-Saclay, 91128 Palaiseau, France

10    5) Laboratoire de Météorologie Dynamique, École Polytechnique, 91128 Palaiseau, France.

11    \* corresponding author: Cheikh DIONE, [cdione@ipsl.fr](mailto:cdione@ipsl.fr)

12    **Abstract:**

13    In this study, we use a synergy of in-situ and remote sensing measurements collected during the Southwest  
14    FOGs 3D experiment for processes study (SOFOG3D) field campaign in autumn 2019 and winter 2020, to  
15    analyze the thermodynamic and turbulence processes related to fog formation, evolution, and dissipation  
16    across southwestern France. Based on a unique dataset with a very high resolution and a fog conceptual  
17    model, an analysis of the four heaviest fog episodes (two radiation fogs and two advection-radiation fogs) is  
18    conducted. The results show that radiation and advection-radiation fogs form under deep and thin  
19    temperature inversion, respectively. For both fog categories, the transition period from stable to adiabatic fog  
20    and the fog adiabatic phase are driven by vertical mixing associated with an increase in turbulence in the fog  
21    layer due to mechanical production (turbulence kinetic energy (TKE) up to  $0.4 \text{ m}^2 \text{ s}^{-2}$  and vertical velocity  
22    variance ( $\sigma_w^2$ ) up to  $0.04 \text{ m}^2 \text{ s}^{-2}$ ) generated by brisk wind at the supersite (advection). The dissipation time is  
23    observed at night for the advection-radiation fog case studies and during the day for the radiation fog case  
24    studies. Night-time dissipation is driven by horizontal advection generating mechanical turbulence (TKE at  
25    least  $0.3 \text{ m}^2 \text{ s}^{-2}$  and  $\sigma_w^2$  larger than  $0.04 \text{ m}^2 \text{ s}^{-2}$ ). Daytime dissipation is linked to the combination of thermal  
26    and mechanical turbulence related respectively to solar heating (near surface sensible heat flux larger than  $10$   
27     $\text{W m}^{-2}$ ) and advection. Through a deficit of the fog reservoir of liquid water path, the fog conceptual model  
28    estimates the dissipation time at least one hour before the observed dissipation for radiation fog cases. It  
29    gives a better estimate of the fog dissipation time for advection-radiation cases. This study also demonstrates  
30    the importance of using instrumental synergy (with microwave radiometer, wind lidar, weather station, and  
31    cloud radar) and a fog conceptual model to better predict fog characteristics and dissipation time at  
32    nowcasting ranges.

33

34    **Key words:** Fog conceptual model, radiation/advection fog, fog life cycle, turbulence, Southwestern France,  
35    SOFOG3D



## 36 **1. Introduction**

37 Fog is an extreme meteorological phenomenon forming in several regions of earth under  
38 different atmospheric conditions depending on the season and location (Gultepe et al., 2007). It is  
39 defined by the suspension of water droplets in the lowest troposphere which reduces the horizontal  
40 visibility to lower or at least 1000 m. Fog has significant negative impacts on air, road and marine  
41 traffic causing large economical and human losses (Bartok et al., 2012, Bartoková et al., 2015,  
42 Huang and Chen, 2016). It also has a high impact on solar energy, particularly in the mid-latitudes  
43 during Autumn and Winter. Based on in-situ measurements, several studies have focused on fog  
44 formation at different regions and highlighted the main processes leading to its initiation allowing to  
45 define four categories of fog: radiation fog (Price 2019), advection-radiation fog (Gultepe et al.,  
46 2007, 2009; Niu et al., 2010a, b, Dupont et al., 2012), advection fog (Koračin et al., 2014; Liu et al.,  
47 2016, Fernando et al., 2021), and precipitation fog (Tardif and Rasmussen, 2007; Liu et al., 2012).  
48 According to the literature, several processes are identified to drive fog evolution and dissipation  
49 depending on each category. Fog formation requires low intensity of turbulence (Nakanishi 2000;  
50 Bergot 2013; Price 2019)

51 Dhangar et al., 2021 found that optically thin fog develops under low-turbulence kinetic energy and  
52 the transition to dense fog is observed when the turbulence increases and reaches enough values to  
53 allow the vertical mixing of the fog layer. The dissipation of radiation fog is usually observed after  
54 sunrise and linked with the increase in solar heating leading to the evaporation of water drops and a  
55 vertical mixing of water vapor (Roach, 1995; Haeffelin et al., 2010; Maalick et al., 2016). Bergot et  
56 al., 2015 relied on large eddy simulations (LES) to characterize the role of dry downdrafts in  
57 allowing solar radiation to reach the ground and increasing the turbulence. Additionally, Pauli et al.,  
58 2022 studied the climatology of fog and low stratus cloud formation and dissipation times in  
59 Central Europe using satellite data and showed that fog dissipation is also often related to  
60 topography. The dissipation processes are more difficult to study than the fog formation processes,  
61 due to the complexity of fog's scale. At the state of the art, based on case studies, numerical  
62 weather prediction models (Philip et al., 2016, Bell et al., 2022) and high resolution models (Price  
63 et al., 2018, Ducongé et al., 2020, Fathalli et al., 2022) up to LES (Bergot et al., 2015, Mazoyer et  
64 al., 2017) have the ability to simulate fog formation in several complex areas. However, they have  
65 difficulties in simulating the processes driving fog evolution over land in real time (Steenefeld *et*  
66 *al.*, 2015, Price et al., 2015, Román-Cascón et al., 2016; Wærsted et al., 2019; Pithani et al., 2020,  
67 Boutle *et al.*, 2022).



68 Toledo et al., 2021 developed a one-column conceptual model of adiabatic continental fog  
69 allowing to define key fog metrics as the equivalent fog adiabaticity by closure and the reservoir of  
70 liquid water path (RLWP) that can be estimated in real-time and allowing a diagnostic of fog  
71 evolution. Based on seven years of measurements collected at SIRTÀ (Site Instrumental de  
72 Recherche par Télédétection Atmosphérique), a French observatory located at Palaiseau/France,  
73 Toledo et al., 2021 have validated their model on the timing of fog dissipation based on the RLWP.  
74 The limitation of this model is that the estimation of the reservoir depends on fog specific  
75 parameters and does not take into account local (turbulence) or large scale processes (advection).  
76 Indeed, to further understand uncertainties associated with the estimation of the RLWP, the  
77 validation of the model using data from other measurement sites having a large occurrence of fog is  
78 another step before using it in nowcasting ranges.

79 Understanding the life cycle of fog is an imperative for numerical weather prediction models  
80 in order to set up an effective and efficient early warning system to reduce the socio-economic  
81 impacts of this phenomenon in areas with high occurrence of fog. Thus, finding the right  
82 instruments on which this warning system will be based is also another challenge that can be partly  
83 resolved by field campaigns combining both in-situ and remote sensing measurements and  
84 numerical simulations. At the state of the art, nowcasting fog requires more efforts in in-situ  
85 measurements and modeling. In this context, the SOuth westFOGs 3D (SOFOG3D) project, led by  
86 Météo-France, was designed to document local processes involved in fog formation, evolution and  
87 dissipation to better improve its predictability in numerical weather prediction models in the  
88 Southwestern France.

89 In order to improve our understanding of the processes driving the fog life cycle and to validate the  
90 fog conceptual model from Toledo et al., 2021 on another region than the one on which it has been  
91 developed, the current study aims at identifying the main dynamical and thermodynamic processes  
92 driving fog's formation, evolution, and dissipation in the framework of SOFOG3D project. Using  
93 an instrumental synergy of in-situ and remote sensing measurements and the fog conceptual model,  
94 the phenomenology of fog and the different phases driving its evolution are deeply analyzed  
95 considering four heavy fog case studies observed over Southern France during Winter 2019-2020.

96 This paper is structured into five sections. The datasets and methodological approach are  
97 described in the following section. Section 3 gives an analysis of the processes involved in fog  
98 evolution based on two different categories of fog formation phenomenology. Section 4 of this



99 manuscript includes a discussion on the thermodynamical and turbulent processes driving the fog  
100 phases and Section 5 presents the conclusion.

## 101 **2. Data and methodology**

102 In a mesoscale context, the SOFOG3D field experiment is located in Southwestern France,  
103 in the Aquitaine region (Fig. 1a). The field campaign was carried out during the Autumn 2019 and  
104 Winter 2020 period leading to 15 intensive observation periods (IOPs). A unique dataset has been  
105 collected across a complex region with a very contrasted topography. This region is bordered in the  
106 east by the “Massif Central”, in the west by the Atlantic Ocean, in the north by Bordeaux and in the  
107 south by the “Pyrenees”. In the region, several dynamical effects can be observed such as sea  
108 breeze, land breeze, and mesoscale foehn circulations influencing the fog life cycle. At the local  
109 scale, the supersite under focused here is bordered by two rivers: “La Garonne” to the East and  
110 “L’Eyre” to the west (Fig. 1a). These two rivers and the surrounding surface heterogeneities can  
111 modulate the fog formation and dissipation times. During the campaign, several in-situ and remote  
112 sensing measurements were jointly deployed in the studied area of SOFOG3D. In this paper, our  
113 analysis focuses on the data collected in the surroundings of the supersite at Charbonnière, the most  
114 instrumented site (Fig. 1b) during the field campaign. Below, the descriptions of the in-situ and  
115 remote sensing measurements and then the fog conceptual model are presented with emphasis on  
116 the main meteorological variables used in the study.

### 117 **2.1 Dataset**

#### 118 **2.1.1 Surface measurement data**

119 A network of surface weather stations was installed in the study domain of SOFOG3D at the  
120 vicinity of Charbonnière, to document the spatial variability of fog and surface heterogeneities at  
121 the local scale (Fig. 1b). Four weather stations were also deployed around the supersite in a  
122 northeast-southwest transect (Fig. 1b). These stations were installed at Moustey, Cape Sud, Tuzan  
123 and Noaillan, almost at the same altitude, and operated continuously with very high temporal  
124 resolution (0.1 s time interval) during the period from 18 October 2019 to 31 December 2020. In  
125 addition to temperature, pressure, relative humidity sensors and anemometer, a scatterometer  
126 provided the visibility used to estimate fog formation and dissipation times at each station.  
127 Temperature data are used to characterize the spatial variability of the radiative cooling. Wind



128 speed and direction are used to get an indication of the local circulations and their association with  
129 air mass advection (spatial coherence of wind) and source of turbulence.

130 In this study, fog occurrence is defined using the visibility at the supersite based on an  
131 algorithm developed by Tardif and Rasmussen, 2007. This algorithm consists of dividing visibility  
132 time series into 10 min blocks. A fog block means that half of the visibility measurements during a  
133 10 min period are below 1000 m. Blocks are characterized by a positive or negative construct. A  
134 positive construct indicates that five consecutive blocks of which the central block is fog and at least  
135 two other blocks are also fog blocks. The opposite means a negative construct. Thus, the fog  
136 formation time corresponds to the first fog block in the first positive construct encountered. The fog  
137 dissipation time corresponds to the last fog block in the last positive construct before either a  
138 negative construct or three consecutive non-fog blocks are encountered. This algorithm discards fog  
139 events shorter than 1 hour.

140 Météo-France installed in a fallow field near the supersite, several sensors as Licor analyzers  
141 and sonic anemometers to continuously measure the near-surface (3 m a.g.l) meteorological  
142 conditions (air temperature and relative humidity) and pressure at 0.3 m a.g.l) and the three  
143 components of the wind at 10 m a.g.l. These instruments provided high frequency data at 20 Hz. In  
144 this study, to document fog dissipation processes, we use sensible heat flux (SHF), turbulence  
145 kinetic energy (TKE), and vertical velocity variance ( $\sigma_w^2$ ). These variables are estimated using the  
146 Eddy-covariance methods (Foken et al., 2004, Mauder et al., 2013) calculated every 30 minutes  
147 after a high quality control of the data. More details on the data can be found in Canut, 2020.

### 148 **2.1.2 Observation of cloud characteristics**

149 For the monitoring of cloud layers, a BASTA cloud radar (Delanoë et al., 2016) was  
150 deployed at Charbonnière and a CL51 Ceilometer at Tuzan (7.4 km northwest of Charbonnière)  
151 (Fig. 1b).

152 BASTA is a 95-GHz cloud radar manufactured by the Laboratoire Atmosphères, Milieux,  
153 Observations Spatiales (LATMOS) with an absolute calibration method for frequency-modulated  
154 continuous wave (FMCW) cloud radars based on corner reflectors (Toledo et al., 2020). From 7  
155 November 2019 to 12 March 2020, the radar was operated continuously with a vertical pointing  
156 mode having three vertical resolutions (12.5 m, 25 m, and 100 m). It provided radar reflectivity and  
157 Doppler velocity. The lowest mode, having its first available gate at 37.5 m a.g.l and 12.5 m of  
158 vertical resolution, is used to estimate the cloud top height (CTH) which gives the fog thickness at a



159 time resolution of 30 seconds. It also provides the level of highest concentration of droplets in the  
160 fog layer. The CTH is estimated using a radar reflectivity threshold of -34 dBZ.

161 The CL51 is manufactured by Vaisala and automatically provided three estimates of cloud  
162 base height (CBH) allowing the detection of cloud decks every 30 seconds with a vertical resolution  
163 of 15 m. from 10 October 2019 to 2 April 2020. In this study, we use the lowest CBH, which  
164 corresponds to the base height of stratus cloud lowering or lifting when fog forms or dissipates,  
165 respectively. More information on the data provided by the CL51 can be found in Burnet, 2021.

### 166 **2.1.3 Temperature and wind profiling**

167 A microwave radiometer Hatpro (MWR) manufactured by Radiometer Physics GmbH  
168 (RPG) was installed at the supersite to characterize thermodynamic atmospheric conditions during  
169 the field campaign. From 4 December 2019 to 9 May 2020, the MWR operated continuously at the  
170 supersite using two spectral-bands: the K-band which 22.24-31 GHz used for the retrieval of  
171 humidity profiles, integrated water vapor (IWV) content and liquid water path (LWP), and the V-  
172 band which 51-58 GHz to retrieve temperature profiles. In order to improve the vertical resolution  
173 in the boundary layer, the MWR was set up to scan in 10 elevation angles every 10 minutes with a  
174 zenith pointing each 1 second. Using neural networks, brightness temperatures measured by the  
175 MWR are inverted to temperature and humidity variables. More details on this method can be found  
176 in Martinet et al., 2022. Comparing temperature and humidity profiles retrieved by the MWR with  
177 radiosonde data, Martinet et al., 2022 found that air temperature has cold biases below 0.5 K in  
178 absolute value below 2 km but increases up to 1.5 K above 4 km altitude. The low biases in the  
179 lowest atmosphere allow a good estimation of the lowest temperature inversion under focus in this  
180 study. For each case study, the transition from stable to adiabatic fog is estimated using the static  
181 atmospheric stability in the lowest atmosphere computed using the temperature profile. The air  
182 temperature profiles are also used to characterize the atmospheric conditions linked to the  
183 development of fog at Charbonnière. For the absolute humidity, the maximum dry bias of the MWR  
184 is around  $1.4 \text{ g m}^{-3}$  in the lowest troposphere up to 1.7 km and becomes wet above ( $0.3 \text{ g m}^{-3}$ ). The  
185 small biases in humidity profiles shows that the LWP accuracy is in the scope of those defined in  
186 the literature (Crewell and Löhnert, 2003; Marke et al., 2016). The LWP is a key parameter to  
187 consider for the microphysical characteristics of fog and is used in the conceptual model. More  
188 information regarding the data can be found in Martinet, 2021.



189           The WindCube lidar becomes a common instrument used in documenting very low  
190 atmospheric phenomena such as turbulence (Liao et al., 2020; Kumer et al., 2016). Dias Neto et al.,  
191 2023 demonstrated the usefulness of the wind speed and direction estimated using the WindCube  
192 V2. Comparing wind from WindCube V2 with GPS radiosonde, they found low biases of  $0.52 \text{ m s}^{-1}$   
193 and  $0.37^\circ$  for the wind speed and direction, respectively. To investigate the dynamics of the  
194 atmosphere at the supersite, a WindCube V2 lidar manufactured by Leosphere was deployed by  
195 Météo-France during the field campaign to provide from 1 October 2019 to 10 April 2020, the wind  
196 measurements at 10 levels ranging from 40 m to 220 m above ground level (a.g.l). The  
197 measurements made at a 1 Hz frequency and a 20 m vertical resolution provided the estimation of  
198 turbulence parameters such as the turbulent kinetic energy (TKE). The TKE is computed every 30  
199 minutes using the horizontal wind component at the high resolution. It is used in this study to  
200 analyze the role of turbulence within the foggy-layer to further characterize fog formation,  
201 evolution, and dissipation. More details on the WindCube lidar data can be found in Canut et al.,  
202 2022.

#### 203 **2.1.4 Fog adiabaticity and reservoir**

204           To further understand fog characteristics, it is essential to focus our analysis on several  
205 variables related to the formation, evolution and dissipation of fog. Fog adiabaticity and reservoir  
206 are key metrics driving the life cycle of fog. They are estimated using the fog conceptual model  
207 (Toledo et al., 2021) developed at SIRTa. This model is a uni-dimensional model inspired by  
208 previous numerical models for stratus clouds (Betts, 1982, Albrecht et al., 1990; and Cermak and  
209 Bendix, 2011). The basic hypothesis is to consider a well-mixed fog layer and to express the  
210 increase in height of the fog liquid water content as a function of the local adiabaticity and the  
211 negative of the change in the saturation mixing ratio with height ( $\Gamma_{\text{ad}}(T,P)$ ) (equation A1). Fog  
212 liquid water path is parameterized as a function depending on the equivalent fog adiabaticity ( $\alpha_{\text{eq}}$ )  
213 and the CTH (equation A3). The equivalent fog adiabaticity is used to characterize the buoyancy in  
214 low clouds.  $\alpha_{\text{eq}}$  varies depending on the in-cloud mixing parameter  $\beta$  and is expressed as  $\alpha_{\text{eq}} = (1-\beta)$   
215 (Betts, 1982 and Cermak and Bendix, 2011). For low-level clouds, as stratus and stratocumulus,  $\alpha_{\text{eq}}$   
216 is between 0.6 and 0.9 (Braun et al., 2018) indicating sufficient buoyancy in the cloud layer with an  
217 adiabatic profile. To parameterize this parameter in the fog conceptual model, Toledo et al., 2021  
218 used an inversion of Eq. (A3) to define a fog adiabaticity from closure ( $\alpha_{\text{eq}}^{\text{closure}}$ ) given in equation  
219 (1).  $\alpha_{\text{eq}}^{\text{closure}}$  depends on the accumulated liquid water content (LWC) at the fog base ( $\text{LWC}_0$ ), fog





220 thickness (e.g. CTH), the LWP and the adiabaticity. The adiabaticity lapse rate is a function of air  
221 temperature and pressure. Toledo et al., 2021 found that the equivalent fog adiabaticity from closure  
222 is negative when the LWP is below  $30 \text{ g m}^{-2}$ . They defined the transition phase from stable to  
223 adiabatic conditions when the equivalent fog adiabaticity from closure is around 0.5. In the  
224 conceptual model, this parameter is estimated only for a CTH below 462.5 m with free cloud above.

$$225 \alpha_{eq}^{closure} = \frac{2(LWP - LWC_0 CTH)}{\Gamma_{ad}(T, P) CTH^2} \quad (1)$$

226 Considering that adiabatic fog exists because the liquid water path in its thickness is strictly  
227 greater or equal to its critical liquid water path (CLWP) (Toledo et al., 2021), it is possible to define  
228 an associated quantity named the fog reservoir of liquid water path (RLWP). The RLWP is defined  
229 as the difference between fog current liquid water path and the critical value, as shown in equation  
230 2. It depends on the critical liquid water content (LWC<sub>c</sub>) (A.4), the adiabaticity and fog thickness.  
231 The calculation of fog RLWP can be used to anticipate the dissipation or thickening of the fog in  
232 the coming minutes or hours. Based on 20 fog cases at SIRTA, Toledo, 2021 found that for a  
233  $RLWP > 30 \text{ g m}^{-2}$  in a given time instant, fog does not dissipate within the following 30 minutes. He  
234 also showed that the RLWP trend decreases before fog dissipation time and increases when fog is  
235 persisting. This behavior motivates the analysis of the RLWP trend in this study to improve the  
236 characterization of the different fog phases.

$$237 RLWP = LWP - CLWP = LWP - \frac{1}{2} \alpha_{eq} \Gamma_{ad}(T, P) CTH^2 - LWC_c CTH \quad (2)$$

238 The number of fog events observed during the SOFOG3D field campaign is not sufficient to  
239 calibrate the fog conceptual model in southeastern France as in SIRTA (Toledo et al., 2021). In this  
240 study, we use the model with its parametrization at SIRTA to further characterize the different  
241 phases observed in the lifetime of fog based on single identified case studies. The model is  
242 performed when the visibility is lower than 1000 m.  $\alpha_{eq}^{closure}$  is used to characterize the fog transition  
243 from stable phase to adiabatic phase. The RLWP gives information about the predictability of fog  
244 dissipation time at nowcasting range. More details on the fog conceptual model is given in  
245 appendices and can be found in Toledo, 2021.

## 246 2.2 Case studies and methodological approach

247 For the whole SOFOG3D campaign, based on the fog defined criteria described in section  
248 2.2.1, 31 fog events are identified during 31 October 2019 - 26 March 2020 period. For each one, a



249 visual expectation of the time-height cross-section of the radar reflectivity from BASTA cloud radar  
250 and the cloud base height from the Ceilometer was carried out. We selected the four most  
251 developed fog episodes, namely case studies 1 (IOP 5), 2 (IOP 6), 3 (IOP 11) and 4 (IOP 14).

252 As in Toledo et al., 2021 (their Fig. 3), Figure 2 shows the equivalent adiabaticity by closure  
253 versus LWP and CTH for the 4 fog case studied. It indicates that  $\alpha_{\text{eq}}^{\text{closure}}$  reaches 0.5 when LWP  
254  $> 20 \text{ g m}^{-2}$  and the CTH  $> 150 \text{ m}$  which should be the conditions favorable for the fog to become  
255 optically opaque to the infrared radiation. At the supersite, the LWP observed during that transition  
256 is lower than the threshold at SIRT (LWP  $> 30 \text{ g m}^{-2}$ ) (Wærsted et al., 2017 and Toledo et al.,  
257 2021). However, there is a consistency between both sites on the computation of the equivalent  
258 adiabaticity by closure. This legitimises the choice of the four days, and motivates the use of the  
259  $\alpha_{\text{eq}}^{\text{closure}}$  in this study to define the transition phase between stable and adiabatic fog.

260 For the selected case studies, Table 1 contains the fog formation and dissipation times, fog  
261 formation types, and fog duration at the supersite. For all selected fog events, the formation time of  
262 fog is observed between 20:40 and 22:40 UTC and the dissipation time varies from night to  
263 daytime. These selected fogs triggered by radiation (2 cases) or advection-radiation (2 cases)  
264 processes.

265 For each selected case study, temperature profiles from the MWR, radar reflectivity profiles  
266 from the BASTA cloud radar and the equivalent fog adiabaticity derived from the conceptual model  
267 are used to define the four fog phases characterizing the fog evolution: fog pre-onset, stable fog,  
268 adiabatic fog, and fog dissipation. Note that an important time of the fog life cycle is the transition  
269 time between stable and adiabatic fog. Each fog phase is defined as following:

270 1/ Fog pre-onset is defined as the two hours preceding fog onset associated with cloud free  
271 conditions.

272 2/ In the four cases studies, the stable phase starts at fog onset. It is characterized by a stable  
273 temperature profile in the lowest 100 m of the atmosphere.

274 3/ The transition time separating the stable and adiabatic phases can be defined differently  
275 depending on the meteorological variables considered. Price et al., 2011 defined this transition time  
276 as the time when the air temperature is constant in the fog lowest layer (1.5 - 50 m a.g.l). Toledo et  
277 al., 2021 found that the transition is observed when the equivalent fog adiabaticity by closure is  
278 increasing between 0 and 0.5. In this study, for a better definition of this period, we take into  
279 account the static stability given by the hourly profiles of mean air temperature from the MWR, the  
280 fog geometry (CTH) from the cloud radar, and the  $\alpha_{\text{eq}}^{\text{closure}}$  from the conceptual model. Indeed, the



281 transition period is defined as the time when the temperature profile becomes unstable or neutral in  
 282 the 0-75 m a.g.l layer, while the fog CTH increases with time, and  $\alpha_{eq}^{closure}$  increases from 0 to about  
 283 0.5. Note that the thickening of the fog is associated with the elevation of the level of the maximum  
 284 radar reflectivity. The transition phase starts when  $\alpha_{eq}^{closure} < 0.5$ , the CTH suddenly increases more  
 285 than 25 m in 5 minutes under a stable or neutral layer. This phase ends when  $\alpha_{eq}^{closure}$  reaches 0.5 and  
 286 the fog layer becomes neutral or unstable.

287 4/ Fog adiabatic phase is characterized by  $\alpha_{eq}^{closure}$  around 0.5, a neutral or unstable  
 288 temperature profile, and a radar reflectivity that increases with increasing altitude and peaks a few  
 289 tenths of meters below cloud top.

290 5/ Fog dissipation phase is defined as being the period between 30 minutes before and after  
 291 dissipation time (when horizontal visibility becomes greater than 1 km). Since the fog dissipation  
 292 time does not appear abruptly, as it is driven by thermodynamical processes, we consider this time  
 293 range to further document them.

294 Based on these fog phase definitions, in the following, we describe the four case studies. For  
 295 each fog event, we document, using the fog conceptual model and the instrumental synergy, the  
 296 processes involved in the evolution of fog in each of these phases, in order to identify the main  
 297 processes driving the fog life cycle.

298 **Table 1** : Case study number, fog onsets, type of fog formation, fog dissipation times, fog duration  
 299 and type of fog dissipation for the four documented case studies. Time is in UTC. Dates are in the  
 300 format “dd/mm/yyyy”. “dd” indicates the day, “mm” the month and “yyyy” the year.

Case study number	Formation time		Fog types	Dissipation time		Fog duration (hh:min)
	Date	Hours		Date	Hours	
	dd/mm/yyyy	(UTC)		dd/mm/yyyy	(UTC)	
1	28/12/2019	22:40	Radiation	29/12/2019	11:00	12:20
2	05/01/2020	20:40	Radiation	06/01/2020	08:40	12:00
3	08/02/2020	20:40	Advection-radiation	09/02/2020	03:40	7:00
4	07/03/2020	21:20	Advection-radiation	08/03/2020	04:00	6:40

301 **3. Fog formation, evolution, and dissipation processes**

302 **3.1 Case study 1 (IOP 5) analysis**



303            Figures 3a and 3b indicate the time-cross sections of the radar reflectivity estimated from  
304 BASTA cloud radar during case study 1, on the 28-29 December 2019, respectively up to 600 m  
305 and 12000 m. They show a clear sky before fog formation time at 22:40 UTC on 28 December  
306 2019. During fog evolution, cloud free conditions are observed above the fog top height until 09:00  
307 UTC when sparse thin high-altitude clouds occur above the cloud radar. Figure 3c presents a quasi-  
308 homogeneous fog formation time between the three sites and heterogeneous dissipation time. At  
309 Charbonnière, fog dissipated at 11:00 UTC, on 29 December 2019 and two hours earlier at  
310 Noaillan. At all sites, low temperatures below 4 °C (Fig. 3e) are observed during the fog period.  
311 Near the surface, light wind ( $< 1 \text{ m s}^{-1}$ ) are recorded at all sites from fog pre-onset to fog  
312 stable/adiabatic transition times (Fig. 3d and 3f).

313            The fog pre-onset is marked by a double stratification of the atmospheric boundary layer  
314 with a thin inversion from surface up to 100 m and deep and strong inversion ( $14 \text{ °C km}^{-1}$ ) above  
315 (Fig. 4a). Atmospheric conditions are dominated by an easterly wind that reaches  $5 \text{ m s}^{-1}$  above 100  
316 m a.g.l which could be considered as a nocturnal low-level jet (Fig. 4d). The mean cooling rate near  
317 the surface is  $-0.9 \text{ °C h}^{-1}$ . The strong decrease in temperature is associated with surface radiative  
318 cooling (cloud free), negative SHF ( $-0.23 \text{ W m}^{-2}$ ) (Fig. 4h), near surface low wind ( $0.61 \text{ m s}^{-1}$ ) (Fig.  
319 3d and 3f) and very low thermal turbulence ( $\text{TKE} = 0.18 \text{ m}^2 \text{ s}^{-2}$  and  $\sigma_w^2 = 0.002 \text{ m}^2 \text{ s}^{-2}$ ). These  
320 conditions lead to thermally-stable atmospheric conditions which are favorable for fog formation  
321 (Table 1). The fog onset slightly precedes the minimum of SHF.

322            The fog stable phase lasts around 6 h (22:50 - 05:00 UTC). Near the surface, it is  
323 characterized on average by a very low radiative cooling rate ( $-0.18 \text{ °C h}^{-1}$ ), an almost zero SHF, an  
324 easterly light wind ( $0.78 \text{ m s}^{-1}$ ), low turbulence ( $\text{TKE} = 0.12 \text{ m}^2 \text{ s}^{-2}$ ,  $\sigma_w^2 = 0.01 \text{ m}^2 \text{ s}^{-2}$ ), and a negative  
325  $\alpha_{\text{eq}}^{\text{closure}}$  ( $-1.3$ ) (Fig. 4e), a low LWP of  $2.18 \text{ g m}^{-2}$  (Fig. 4g), a slight increase in time of the fog  
326 thickness up to 50 m, and a relatively stable temperature inversion height. During this phase,  
327 turbulence, LWP and RLWP are sufficiently low to maintain thermally-stable fog with an horizontal  
328 visibility of 736 m on average.

329            For this case, the transition time from stable fog to adiabatic fog is observed between 05:00  
330 and 07:00 UTC at the supersite. It corresponds to the lowest visibility (198 m) and is illustrated by a  
331 transition in the vertical profiles of air temperature (Fig. 4a) from stable at 05:00 to unstable at  
332 06:00 UTC. The transition is materialized by a deepening of the cold layer. At 05:00 UTC the  
333 coldest temperature is at the surface. At 06:00 UTC, the minimum temperature is observed at 50 m  
334 a.g.l. At that time, the vertical profile of radar reflectivity increases with height, indicating a vertical



335 development of fog (Fig. 4b). At the end of this phase,  $\alpha_{\text{eq}}^{\text{closure}}$  reaches 0.5 which is consistent with  
336 the threshold obtained at the SIRTA site by Toledo et al., 2021. The mean SHF reaches  $4.4 \text{ W m}^{-2}$   
337 and around  $10 \text{ W m}^{-2}$  at the phase end (Fig. 4h). The wind speed at 10 m a.g.l increases to  $1.14 \text{ m s}^{-1}$   
338 and shifts in direction from East to Southeast. The TKE remains constant and the  $\sigma_w^2$  significantly  
339 increases to  $0.01 \text{ m}^2 \text{ s}^{-2}$ . Vertical velocity variance values observed are higher than the threshold  
340 fixed by Price et al., 2019 for a thermally-stable surface layer. This increase in turbulence indicates  
341 a vertical mixing in the fog layer. The LWP and RLWP peak at the end of the transition phase  
342 consistently with a decrease in visibility. Due to the simultaneous increase in SHF, TKE and  $\sigma_w^2$ ,  
343 the transition phase is driven by both thermal and mechanical turbulence.

344 The fog adiabatic phase is observed between 07:00 and 11:00 UTC (4 h duration) at the  
345 supersite. This phase is characterized by a vertical development of fog up to 185 m (Fig. 4b) and the  
346 arrival of sparse high clouds (Fig. 3a and 3b) associated with the lowering of the temperature  
347 inversion top height above the fog top (Fig. 4c). Note that these clouds have no effect on the  
348 radiative cooling at the top height of the fog. The fog layer becomes warmer ( $+0.77 \text{ }^\circ\text{C h}^{-1}$  on  
349 average) and its LWP and RLWP reach  $26.16 \text{ g m}^{-2}$  and  $+6.38 \text{ g m}^{-2}$ , respectively. The turbulence  
350 gradually increases in the fog layer (Fig. 4f) ( $\text{TKE} = 0.28 \text{ m}^2 \text{ s}^{-2}$ ) due to an increase of the horizontal  
351 wind speed ( $2.4 \text{ m s}^{-1}$ ) and its shift from southeasterly to easterly (Fig. 4d). In the same way, the  
352 vertical velocity variance increases to  $0.04 \text{ m}^2 \text{ s}^{-2}$  and is driven by the vertical wind shear and the  
353 increase in SHF ( $12.9 \text{ W m}^{-2}$ ) (Fig. 4h). For this case study, the moderate mechanical and thermal  
354 turbulence causes vertical mixing in the fog layer, which slightly increases the surface horizontal  
355 visibility (370 m).

356 At the supersite, the fog dissipates after sunrise under cloud free atmosphere above its top  
357 height. The SHF continues to increase (Fig. 4h) due to solar radiation. During this phase, the RLWP  
358 becomes negative ( $-11.39 \text{ g m}^{-2}$ ) when the CTH increases significantly, in spite of the increase of  
359 the LWP (maximum of  $43.34 \text{ g m}^{-2}$ ), while  $\alpha_{\text{eq}}^{\text{closure}}$  remains around 0.63. Based on the RLWP, the  
360 fog conceptual model would predict a deficit of liquid water in the fog layer one hour before the  
361 lifting of its base height (Fig. 4g). The fog dissipation phase is induced by the increase of the  
362 vertical mixing generated by the thermal and mechanical turbulence associated with TKE values  
363 larger than  $0.4 \text{ m}^2 \text{ s}^{-2}$  (Fig. 4f). The fog dissipation phase is marked by the daytime atmospheric  
364 convection associated with significant SHF ( $22.02 \text{ W m}^{-2}$ ) generating thermal turbulence ( $\sigma_w^2 = 0.06$   
365  $\text{m}^2 \text{ s}^{-2}$ ), which allows more vertical mixing and warming of the daytime atmospheric boundary layer.



366 In summary, for this fog event, the fog conceptual model is consistent with the in-situ  
367 measurements of turbulence on the timing of the different fog phases. It has provided additional  
368 elements for understanding the different phases of the fog life cycle.

369

### 370 **3.2 Case study 2 (IOP 6) analysis**

371 Radar reflectivity time-cross sections derived from BASTA cloud radar during case study 2 (IOP 6)  
372 on the 5-6 January 2019 indicate that clear weather precedes fog formation at 20:40 UTC on 5 January 2020  
373 (Fig. 5a and 5b). Fog develops below the dry, warm and cloud free stable atmospheric boundary layer (Fig.  
374 5c). This case presents a spatial variability of fog formation time. The fog lasts 12 h and completely  
375 dissipates around 08:40 UTC, on 6 January 2020 at the supersite (see Table 1), while it dissipates earlier at  
376 Noaillan at 04:30 UTC. At all sites in the studied area, cold atmospheric conditions prevailed during the  
377 whole episode (Fig. 5e). The surface wind speed is moderate ( $< 3 \text{ m s}^{-1}$ ) and quite homogeneous in the  
378 studied area (Fig. 5d and 5f). The wind direction changed several times during the fog's evolution.

379 As in case study 1, before fog formation, hourly vertical profiles of temperature from the  
380 MWR (Fig. 6a) indicate a double stratification of the low atmosphere under an easterly low-level jet  
381 (Fig. 6d). Near surface air temperature is negative (Fig. 5e) and indicates frozen surface. These  
382 conditions are associated with an anticyclonic system across central Europe (not shown). During the  
383 fog pre-onset phase, the mean cooling rate at the supersite is  $-0.7 \text{ }^\circ\text{C h}^{-1}$  (Table 2). The continued  
384 decrease in temperature combined with the negative surface SHF ( $-0.17 \text{ W m}^{-2}$ ), southerly very low  
385 wind ( $0.2 \text{ m s}^{-1}$ ) at near surface, very low vertical velocity variance ( $\sigma_w^2 < 0.003 \text{ m}^2 \text{ s}^{-2}$ ) and low  
386 TKE ( $0.06 \text{ m}^2 \text{ s}^{-2}$ ) reveal that atmospheric conditions favorable to fog formation are driven by  
387 surface radiative cooling (Table 1), leading to a thermally-stable surface layer as in case study 1.  
388 Again, the fog onset precedes by a few minutes the minimum of SHF.

389 The fog stable phase is observed from 20:40 UTC to 03:00 UTC (3 h 20 min duration) under  
390 cloud-free conditions above fog top height. It is characterized by a thin fog (71 m) under a very  
391 deep temperature inversion (Fig. 6c), and light varying wind (Fig. 6d). Negative values of the  
392 equivalent fog adiabaticity by closure ( $-0.69$ ) associated with decrease in temperature ( $-0.13 \text{ }^\circ\text{C h}^{-1}$ )  
393 (Fig. 5e), very low mean LWP ( $1.66 \text{ g m}^{-2}$ ) (Fig. 6g), and low turbulence (TKE =  $0.09 \text{ m}^2 \text{ s}^{-2}$  and  $\sigma_w^2$   
394 =  $0.009 \text{ m}^2 \text{ s}^{-2}$ ) are sufficient conditions to maintain a thermally stable, optically-thin fog (242 m of  
395 horizontal visibility), as in case study 1. The continued increase of TKE in the fog layer (Fig. 6f),  
396 and surface SHF (Fig. 6h) triggered the start of the transition phase, limiting the duration of the  
397 stable phase compared to case 1 (IOP 5).



398 For case study 2, the fog transition phase is observed from 00:00 UTC to 02:00 UTC (2 h of  
399 duration) at the supersite (Fig. 6a and 6b). Its characteristics are similar to those found in case study  
400 1 but the LWP ( $7.18 \text{ g m}^{-2}$ ), RLWP ( $+3.55 \text{ g m}^{-2}$ ), cooling rate ( $-0.007 \text{ }^\circ\text{C h}^{-1}$ ) are lower and the  
401 TKE ( $0.23 \text{ m}^2\text{.s}^{-1}$ ) and SHF ( $7.76 \text{ W m}^{-2}$ ) larger. As in case study 1, these turbulent conditions allow  
402 a vertical mixing of the fog layer indicating its transition towards adiabatic fog.

403 Fog adiabatic phase is observed from 02:00 UTC to 08:40 UTC at the supersite. The first  
404 period from 02:00 UTC to 05:00 UTC is marked by a  $\alpha_{\text{eq}}^{\text{closure}}$  larger than 0.5 and a strong increase in  
405 temperature ( $+2 \text{ }^\circ\text{C}$ ), LWP ( $42 \text{ g m}^{-2}$ ), and a positive RLWP until 04:30 UTC. The temperature  
406 inversion above the fog layer strengthened and its top height lowered. The TKE in the fog layer and  
407 the vertical velocity variance continue to increase ( $\text{TKE} > 0.2 \text{ m}^2 \text{ s}^{-2}$  and  $\sigma_w^2 > 0.02 \text{ m}^2 \text{ s}^{-2}$ ). The SHF  
408 oscillates around  $10 \text{ W m}^{-1}$ . These conditions are favorable for the deepening of the fog by vertical  
409 mixing (see Fig. 5a and 6b). The second period from 05:00 UTC to 08:40 UTC is characterized by  
410 the  $\alpha_{\text{eq}}^{\text{closure}}$  lower than 0.5, a decrease in surface temperature, stable base and top height of the  
411 temperature inversion, a sharp decrease in LWP, fog top height and RLWP (oscillating around  $0 \text{ g}$   
412  $\text{m}^{-2}$ ), while the horizontal visibility increases and then decreases again. The decrease in turbulence  
413 ( $\text{TKE} < 0.2 \text{ m}^2\text{.s}^{-2}$ ) is linked to the decrease in wind speed in the fog layer, while the vertical  
414 velocity variance remains significant ( $\sigma_w^2 > 0.02 \text{ m}^2 \text{ s}^{-2}$ ) with positive SHF. During the second half  
415 of the adiabatic phase, the fog layer that contains less than  $20 \text{ g m}^{-2}$  liquid water is not very resilient  
416 to the significant turbulence, as shown by the very low RLWP values and rapidly changing  
417 horizontal visibility.

418 The decrease in LWP seems to be driven by a possible phase change (water droplet to snow  
419 droplets) of the water droplets inducing a cooling in the fog layer and an increase in horizontal  
420 visibility. The dissipation of the mechanical turbulence favors the lowering of the fog thickness.  
421 These processes seem to be linked to the formation of snowflakes in the fog layer with fall due to  
422 their gravity which is consistent with the visual observations of scientists operating at the supersite,  
423 who reported frost on the tethered balloon.

424 As in case study 1, at the supersite, fog dissipates in the morning at 08:40 UTC, around  
425 sunrise. The RLWP predicted the fog dissipation at 07:30 UTC, one hour fifteen minutes before its  
426 total dissipation time. The surface vertical velocity variance became larger than  $0.04 \text{ m}^2 \text{ s}^{-2}$  and the  
427 TKE in the fog layer higher than  $0.4 \text{ m}^2 \text{ s}^{-2}$ , the  $\alpha_{\text{eq}}^{\text{closure}}$  oscillated around 0.5. These atmospheric  
428 characteristics in the fog layer are linked to the increase in turbulence associated with the increase  
429 of the wind speed (Fig. 5d) and the SHF (Fig. 5h), both induced by the convective mixing due to





430 solar radiation. Therefore, as in case study 1, the dissipation of fog is driven by the turbulence  
431 associated with mechanical and thermal processes.

### 432 **3.3 Case study 3 (IOP 11) analysis**

433 Radar reflectivity cross-sections on the 8-9 February 2020 (IOP 11) (Fig. 7a and 7b) indicate  
434 that this fog event is characterized by an early formation of fog at 20:40 UTC. Fog formation is  
435 preceded by a short rain (8.36 mm at Moustey) period produced by a stratocumulus cloud (Fig. 7b).  
436 After the rain, the water vapor in the lowest atmosphere starts to condensate as an ultra-low stratus  
437 cloud due to radiative cooling. From fog formation time up to 03:00 UTC, the sky is clear above the  
438 fog at the supersite. These atmospheric conditions allow a radiative cooling which favors the  
439 stabilization of the surface layer. Figure 7c indicates a spatio-temporal variability of fog formation  
440 time during a period of strong decrease in near surface temperature (Fig. 7e) at the beginning of the  
441 night and relatively light westerly wind (Fig. 7f and 7d). The formation of the fog started from the  
442 West and spread toward the East, illustrating a West-East gradient of fog formation in line with the  
443 westerly wind blowing in the studied area. During fog evolution, there is a spatial heterogeneity of  
444 temperatures up to 4°C between Moustey (western and coldest site) and Noaillan (eastern and  
445 warmest site). On the other hand, the dissipation is fairly homogeneous at all the sites, consecutive  
446 to an increase in air temperature and wind speed, and a shift in the wind direction (south-south-east  
447 to south), except at Noaillan where fog dissipation occurs earlier as visibility and temperature are  
448 higher than at the other sites. The fog dissipates at 03:40 UTC when the low atmosphere becomes  
449 neutral or unstable and the maximum radar reflectivity decreases and jumps in height (Fig. 8b). Just  
450 after the fog dissipation time, high clouds appear around 10 000 m height, characterising the change  
451 in air mass by advection.

452 Figure 8c shows that for this case study, the temperature inversion forms after the formation  
453 of the ultra-low stratus associated with the advection of the westerly Atlantic flow near the ground  
454 (Fig. 8d). The westerly flow brings wet and mild air over land and contributes to reduce the surface  
455 radiative cooling. The temperature inversion formed at the same time as the base of the stratus  
456 touches the ground, justifying the classification of fog formation by advection-radiation processes  
457 (Ryznar, 1977).

458 The formation of the fog considerably modified the dynamics of the low-level atmosphere  
459 by slowing down the radiative cooling, thus creating a thin layer of temperature inversion around  
460 250 m thick with a low intensity of about 3 °C. The fog stable phase is observed from 20:40 UTC





461 and 23:00 UTC at the supersite. It is characterized by a clear sky above the fog top, a decrease in  
462 surface temperature (Fig. 8e) associated with a cooling rate of  $-0.53\text{ °C h}^{-1}$ , negative  $\alpha_{\text{eq}}^{\text{closure}}$  ( $-0.69$ ),  
463 low LWP ( $6.1\text{ g m}^{-2}$ ) (Fig. 8g), low turbulence ( $\text{TKE} = 0.06\text{ m}^2\text{ s}^{-2}$  and  $\sigma_w^2 = 0.002\text{ m}^2\text{ s}^{-2}$ ), and  
464 negative SHF ( $-1.7\text{ W m}^{-2}$ ). As in cases 1 and 2, these atmospheric characteristics allow to maintain  
465 thermally-stable conditions.

466 Figure 8a indicates that the transition stable/adiabatic fog was observed between 23:00 UTC  
467 and 02:30 UTC (03:30 duration). The vertical profiles of radar reflectivity in Fig. 7a are consistent  
468 with the temperature profiles on the fog stable/adiabatic transition time. The transition time  
469 corresponds with the increase in height and intensity of the radar reflectivity. The fog transition is  
470 observed when on average, the visibility is minimum at Charbonnière (185 m), with low and  
471 negative cooling rate ( $-0.08\text{ °C h}^{-1}$ ), low and negative  $\alpha_{\text{eq}}^{\text{closure}}$  ( $-0.21$ ) which are associated a low  
472 LWP ( $12.74\text{ g m}^{-2}$ ) and a RLWP reaching ( $+10\text{ g m}^{-2}$ ) (Table 2 and Fig. 8g). These characteristics of  
473 the transition estimated by the fog conceptual model are not consistent with those found by Toledo  
474 et al., 2021, but agree with the vertical profiles of temperature from the MWR (Fig. 8a) and the  
475 increase in turbulence ( $\text{TKE} = 0.1\text{ m}^2\text{ s}^{-2}$  and  $\sigma_w^2 = 0.008\text{ m}^2\text{ s}^{-2}$ ) and SHF ( $-0.21\text{ W m}^{-2}$ ) in the fog  
476 layer (Fig. 8f) due to a brisk change in wind direction and speed (Fig. 8d). In summary, the  
477 transition is driven by mechanical turbulence.

478 The fog adiabatic phase is observed from 02:30 UTC to 03:40 UTC (1 h 10 min duration) at  
479 the supersite under clear sky above the fog top. It is characterized by a decrease of the temperature  
480 inversion top height, of the RLWP ( $3.45\text{ g m}^{-2}$ ) and the SHF ( $-0.49\text{ W m}^{-2}$ ), and an increase of the  
481 LWP ( $30.7\text{ g m}^{-2}$ ),  $\alpha_{\text{eq}}^{\text{closure}}$  ( $0.54$ ), and cooling rate ( $0.81\text{ °C h}^{-1}$ ), while turbulence is kept constant.  
482 The vertical wind shear in the fog top height (Fig. 8d) generates dynamical instability driving the  
483 vertical mixing that reduces the temperature inversion above the fog top (Fig. 8c) which promotes  
484 the vertical development of the fog layer.

485 A sustainable dissipation is observed at 03:40 UTC. Figure 8d indicates that the dissipation  
486 time is associated with an increase of the wind regime ( $8\text{ m s}^{-1}$ ) from the southeast in the entire low-  
487 level atmospheric column attesting the arrival at the supersite of an advected air mass. This front  
488 carried a warm air mass which increased rapidly the near surface temperature ( $1.34\text{ °C h}^{-1}$ ) and  
489 allowed a deepening of the fog layer (see Fig. 8c). Advected air mass warms the fog layer causing  
490 the evaporation of the fog water droplets and the lifting of the water vapor by the vertical mixing  
491 driven by turbulence ( $\text{TKE} = 0.42\text{ m}^2\text{ s}^{-2}$  and  $\sigma_w^2 = 0.07\text{ m}^2\text{ s}^{-2}$ ). Thus, the combination between the  
492 decrease in RLWP ( $2.03\text{ g m}^{-2}$ ) and SHF ( $-3.02\text{ W m}^{-2}$ ), the increase in  $\alpha_{\text{eq}}^{\text{closure}}$  ( $0.6$ ), surface



493 temperature (coupling between surface and fog), and turbulence, and a brisk wind allows the mixing  
494 of fog layer with dry air above resulting to the evolution as a stratus . The fog dissipation phase is  
495 thus driven by the advection of warm air at the supersite.

#### 496 **3.4 Case study 4 (IOP 14) analysis**

497 As in case study 3 (Fig 7a), the time-cross section of radar reflectivity in Figure 9a indicates  
498 that the water vapor in the lowest atmosphere started to condensate as an ultra-low stratus cloud,  
499 associated with a radiative cooling (IOP 14). Fog formed at the supersite at 21:20 UTC. A stratus  
500 with a base height above the fog top height arrived at around 00:30 UTC corresponding with the fog  
501 vertical extension up to 200 m a.g.l. This cloud is advected from the northwest of the region and is  
502 captured by Meteosat Second Generation (MSG2) (not shown). The first fog dissipation time is  
503 observed at 04:00 UTC. Figure 9b shows that middle-altitude clouds are also observed at the  
504 supersite at around 06:20 UTC. These intermittent clouds contribute to the sustainable dissipation of  
505 the fog at 07:00 UTC by the lifting of its base height. The maximum fog thickness of 300 m is  
506 observed at around 06:00 UTC. In Figure 8c, the time evolution of the visibility at the five sites  
507 shows that the time of fog formation shows a shift from west to east, such as in case study 3.  
508 Surface temperatures are contrasted between sites after fog formation and become similar at 04:00  
509 UTC. From midnight to the fog dissipation time, the near surface wind is also the same at all the  
510 sites and blown southerly with intermittent pulses. For the analysis of the processes involved in the  
511 evolution of this case study, we consider its evolution until its first dissipation at 04:00 UTC.

512 At the supersite, the fog pre-onset phase is characterized by a radiative cooling favoring the  
513 formation of a temperature inversion (Fig. 10c), the occurrence of a westerly wind (Fig. 10d)  
514 transporting mild and wet air from the Atlantic Ocean. The vertical wind shear created by the  
515 increase in wind reduces the intensity of the temperature inversion linked to the radiative cooling ( $-$   
516  $0.48 \text{ }^\circ\text{C h}^{-1}$ ) (Fig. 10a); negative and low SHF ( $-1.17 \text{ W m}^{-2}$ ); low turbulence ( $\text{TKE} = 0.06 \text{ m}^2 \text{ s}^{-2}$  and  
517  $\sigma_w^2 = 0.002 \text{ m}^2 \text{ s}^{-2}$ ) and allows the condensation of water vapor in the very low layers driving the  
518 triggering of the ultra-low stratus being the fog. For this episode, the occurrence of middle and high  
519 clouds and the increase in wind at the supersite attests that the fog pre-onset phase is driven by the  
520 advection and radiative cooling as observed in case study 3.

521 Fog stable phase is observed at the supersite from 21:20 UTC to 23:30 UTC (2 h 10 min  
522 duration) under cloud-free conditions above the fog. It is characterized by a low surface horizontal  
523 visibility (230 m), a negative  $\alpha_{\text{eq}}^{\text{closure}}$  ( $-0.46$ ), a high cooling rate ( $-0.88 \text{ }^\circ\text{C h}^{-1}$ ), a stable temperature



524 inversion with 210 m thickness, low LWP ( $11.34 \text{ g m}^{-2}$ ), negative SHF ( $-3.26 \text{ W m}^{-2}$ ) and low  
525 turbulence ( $\text{TKE} = 0.09 \text{ m}^2 \text{ s}^{-2}$  and  $\sigma_w^2 = 0.012 \text{ m}^2 \text{ s}^{-2}$ ) (see Table 2 and Fig. 10).

526 The transition between stable and adiabatic fog is observed from 23:30 UTC to 01:00 UTC  
527 (1 h 30 min duration) (see Table 2). As in the previous case studies, this phase is well characterized  
528 by the vertical profiles of temperature and radar reflectivity (Fig. 10a and 10b, respectively) as well  
529 as the rapid increase of  $\alpha_{\text{eq}}^{\text{closure}}$  (from -1.0 to +0.5), a positive RLWP ( $+11.93 \text{ g m}^{-2}$ ) associated with  
530 increasing LWP ( $21.19 \text{ g m}^{-2}$ ), moderate turbulence ( $\text{TKE} = 0.19 \text{ m}^2 \text{ s}^{-2}$ ;  $\sigma_w^2 = 0.03 \text{ m}^2 \text{ s}^{-2}$ ), low and  
531 negative SHF ( $-1.52 \text{ W m}^{-2}$ ) and positive cooling rate ( $+0.12 \text{ }^\circ\text{C h}^{-1}$ ) (Table 2). The fog thickness at  
532 that time is 209 m and the visibility 249 m. Therefore, the transition phase is driven by the  
533 mechanical turbulence produced by the brisk horizontal wind at the supersite (Fig. 10d). The  
534 vertical shear associated with the wind allows a vertical mixing in the fog layer contributing to  
535 reduce the temperature inversion. Note that the brisk wind is associated with the arrival of the  
536 stratus above the fog top height (Fig. 9a and 10b).

537 At the supersite, fog adiabatic phase is observed from 00:20 UTC to 04:00 UTC (03:40  
538 duration) during this case study. This phase includes a partial dissipation of the fog from 04:00 to  
539 05:30 UTC. The first part of this phase is marked by an increase of the surface horizontal visibility  
540 (372 m), the deepening of the fog layer (CTH = 292 m) and the arrival of an advected stratus cloud.  
541 This period is characterized by episodic brisk winds of southerly flow (Fig. 9d). These episodic  
542 brisk winds are associated with intermittent turbulence ( $\text{TKE} = 0.22 \text{ m}^2 \text{ s}^{-2}$  and  $\sigma_w^2 = 0.03 \text{ m}^2 \text{ s}^{-2}$ ),  
543 weak temperature inversion, warming of surface layer (positive cooling rate ( $+0.47 \text{ }^\circ\text{C h}^{-1}$ )), weak  
544 positive SHF ( $1.2 \text{ W m}^{-2}$ ), positive RLWP ( $+8.10 \text{ g m}^{-2}$ ), and high LWP ( $43.02 \text{ g m}^{-2}$ ). These  
545 characteristics allow the fog to remain optically thick (see Table 2), as in case study 1 and 2.

546 As in case study 3, the partial nocturnal dissipation of the fog is observed at 04:00 UTC for  
547 this episode. It is characterized by a negative cooling rate ( $-0.14 \text{ }^\circ\text{C h}^{-1}$ ), a slight decrease in LWP  
548 ( $39.74 \text{ g m}^{-2}$ ) and SHF ( $0.82 \text{ W m}^{-2}$ ), negative RLWP ( $-2.32 \text{ g m}^{-2}$ ), moderate turbulence ( $\text{TKE} =$   
549  $0.27 \text{ m}^2 \text{ s}^{-2}$  and  $\sigma_w^2 > 0.04 \text{ m}^2 \text{ s}^{-2}$ ),  $\alpha_{\text{eq}}^{\text{closure}} = +0.6$ , and brisk wind at the supersite (Fig. 10d). This  
550 brisk wind is associated with an increase of the turbulence in the upper levels of the fog layer due to  
551 wind shear. The RLWP indicates that the fog conceptual model estimates fog dissipation time at  
552 04:00 UTC (Fig. 10a) which is consistent with the horizontal visibility (more than 1000 m) and the  
553 maximum value of  $\alpha_{\text{eq}}^{\text{closure}}$ . These characteristics indicate that the first fog dissipation processes are  
554 driven by an advection of southern flow at the supersite, as in case study 3.



555 **4. Discussion**

556 Figure 11 shows for each fog phase, the mean vertical profiles of air temperature from the  
557 MWR and radar reflectivity from the cloud radar. It highlights the thermal characteristics of fog  
558 phases and differences in atmospheric conditions between fog categories: radiation and radiation-  
559 advection fogs.

560 For radiation fog case studies (1 and 2), the atmospheric conditions preceding (two hours  
561 before) fog formation are dominated by a strong and thick temperature inversion (more than 14 °C  
562 and 1000 m) which is associated with anticyclonic conditions over Europe favoring easterly wind  
563 and clear sky across the studied area. These atmospheric conditions allow a strong surface radiative  
564 cooling, negative heat fluxes and cooling of near surface air at a rate of -0.9 and -0.7 °C h<sup>-1</sup> for case  
565 study 1 and 2, respectively. This cooling is associated with low turbulence indicated by low values  
566 of TKE (0.18 m<sup>2</sup> s<sup>-2</sup> in case 1, and 0.06 in case 2) and near surface vertical velocity variance ( $\sigma_w^2 <$   
567 0.003 m<sup>2</sup> s<sup>-2</sup>) which reinforce the surface thermally stable boundary layer (Fig. 11a and 11b)  
568 favoring the triggering of radiation fog. These results are consistent with the definition of radiation  
569 fog proposed by Price, 2019.

570 In advection-radiation fog case studies (3 and 4), two hours before fog formation, a westerly  
571 sea breeze is present, transporting mild wet air from the ocean. Surface heat fluxes are negative,  
572 favoring cooling of the near-surface air (-1 °C h<sup>-1</sup> in case study 3 and -0.5 °C h<sup>-1</sup> in case study 4) and  
573 turbulent mixing is low (TKE < 0.06 m<sup>2</sup> s<sup>-2</sup>). An East-West gradient of formation and dissipation is  
574 observed in line with the westerly synoptic advection of Atlantic inflow. Fog forms earlier in the  
575 West and dissipates later in the East. The combination of advection and radiative cooling favors fog  
576 formation at about 150 m a.g.l as an ultra-low stratus cloud followed by a rapid (less than 30 min)  
577 lowering of the stratus to the surface triggering the onset of the fog in an unstable (case 3) and  
578 neutral (case 4) surface atmospheric boundary layer (Fig. 11c and 11d).

579 The stable phase is characterized by a stable temperature profile and radar reflectivity which  
580 is maximum near the surface and decreases with height (see Fig. 11). The fog remains shallow (less  
581 than 100 m) with a low LWP ranging less than 12 g m<sup>-2</sup> proportional to fog depth (Table 2). The  
582 equivalent fog adiabaticity by closure parameter ( $\alpha_{eq}^{closure}$ ) is typically negative during the stable  
583 phase indicating that the fog is not in an adiabatic phase. The near-surface temperature decreases  
584 very moderately (-0.2 °C h<sup>-1</sup>) in cases 1 and 2, while the air keeps cooling at about -1 °C h<sup>-1</sup> in cases  
585 3 and 4. For the four cases, surface heat fluxes are slightly negative (-3 to 0 W m<sup>-2</sup>) and turbulence  
586 remains low (TKE at about 0.1 m<sup>2</sup> s<sup>-2</sup> and  $\sigma_w^2$  at 0.01 m<sup>2</sup> s<sup>-2</sup>). This phase is characterized by very low



587 LWPs ( $1-2 \text{ g m}^{-2}$  for radiation fogs and  $6-11 \text{ g m}^{-2}$  for advection-radiation fog). For radiation fog  
588 cases, the stable phase lasts around 6 and 4 hours, respectively, while for advection-radiation cases,  
589 it lasts around 2 hours. This is consistent with the strength of the surface inversion of each category  
590 of fog, as shown in Figure 10. These macrophysical characteristics of the fog stable phase are  
591 consistent with those found by Toledo et al., 2021.

592 The transition from stable to adiabatic phases is a key period in the fog life cycle. This  
593 period is well characterized using the macrophysical parameters of the conceptual model, namely  
594 the equivalent fog adiabaticity by closure ( $\alpha_{\text{eq}}^{\text{closure}}$ ) parameter of the fog, the fog geometry (CTH)  
595 and fog LWP. During the transition from stable to adiabatic phases, these three parameters increase  
596 significantly (see Table 2). In particular,  $\alpha_{\text{eq}}^{\text{closure}}$  evolves progressively from negative values towards  
597  $+0.5$  (Toledo et al., 2021). The transition phase lasts from 01:30 to 03:30, however its timing of  
598 occurrence is unpredictable (case 1 at (05:00 - 07:00 UTC), case 2 (00:00 - 02:00 UTC), case 3  
599 (23:00 - 02:30 UTC), and case 4 (23:30 - 01:00 UTC). During this phase, a change is observed in  
600 static stability from stable profiles to neutral and adiabatic profiles (Fig. 11), while the radar  
601 reflectivity profile presents maximum values near the ground that decrease with height (Fig. 11). In  
602 cases 1, 2 and 4, the transition phase is characterized by an increase in turbulence that can explain  
603 the decrease in thermal stability of the fog layer, either shown in the vertical velocity variance ( $\sigma_w^2$   
604  $\geq 0.02 \text{ m}^2 \text{ s}^{-2}$ ) associated with positive surface heat fluxes (cases 1 and 2), or TKE exceeding  $0.3$   
605  $\text{m}^2 \text{ s}^{-2}$ . (cases 2 and 4). In all the cases, the fog LWP increases significantly which allows a more  
606 efficient radiative cooling of the fog layer, hence contributing to the destabilization of the fog layer.  
607 In case 3, the transition phase is not marked by a significant increase in turbulence. The transition is  
608 more progressive than in the other case studies (this phase lasts 03:30), the CTH is only 25 m  
609 deeper on average than during the stable phase, the  $\alpha_{\text{eq}}^{\text{closure}}$  remains low during that phase, and  
610 reaches 0.5 at the end of the transition phase.

611 According to temperature vertical profiles from the MWR, at the end of the transition time  
612 from stable to adiabatic fog, the temperature profile becomes neutral or slightly unstable. This is  
613 consistent with the definition of the transition given by Price et al., 2011. We also find that it is  
614 during this period that the fog reaches its maximum value of RLWP, showing that the LWP  
615 increases beyond the critical liquid water path value, which gives information on the persistence of  
616 fog.

617 For radiation fog case studies, the adiabatic phase lasts 04:00 and 06:40 for case 1 and 2  
618 respectively, maintaining the fog life cycle during the night until after sunrise. In cases 3 and 4, the



619 adiabatic phase is shorter and lasts 01:00 and 03:40, respectively, with a night-time dissipation at  
620 03:40 and 04:00 UTC, respectively. In this fog phase, for radiation fog, the LWP ranges from 22-26  
621  $\text{g m}^{-2}$  with CTH near 190 m a.g.l. The fog is deeper for advection-radiation fog cases with LWP /  
622 CTH at  $30 \text{ g m}^{-2} / 200 \text{ m a.g.l}$  and  $43 \text{ g m}^{-2} / 290 \text{ m a.g.l}$ , respectively (Table 2). The adiabatic phase  
623 is characterized by an equivalent fog adiabatic by closure parameter near or above 0.5, and a  
624 positive but low RLWP. For all the cases except case 3, the adiabatic phase is associated with  
625 moderate turbulence in the fog layer ( $0.2 < \text{TKE} < 0.4 \text{ m}^2 \text{ s}^{-2}$  and  $0.03 < \sigma_w^2 < 0.04 \text{ m}^2 \text{ s}^{-2}$ ) which  
626 indicates significant vertical mixing generating an unstable surface atmospheric boundary layer  
627 (Fig. 11). This finding is consistent with the result of Ju et al., 2020 who based their analysis on one  
628 case study and Ghude et al., 2023, Dhangar et al., 2021 and Zhou and Ferrier, 2008 for more case  
629 studies analysis. In addition, this phase can also be driven by horizontal advection (mesoscale and  
630 synoptic systems) as in the case study 3.

631 This study shows two fog dissipation periods, at night and after sunrise. Daytime dissipation  
632 is observed for radiative fog cases and night-time dissipation for advection-radiation ones. All of  
633 them are observed when  $\alpha_{\text{eq}}^{\text{closure}} > 0.5$ ,  $\text{TKE} > 0.3 \text{ m}^2 \text{ s}^{-2}$ ,  $\sigma_w^2 > 0.04 \text{ m}^2 \text{ s}^{-2}$ , and the LWP  $> 40 \text{ g m}^{-2}$   
634 (except case study 2). For cases 1 and 2, turbulence is thermally driven by positive SHF, while for  
635 cases 3 and 4, the night-time turbulence increase is mechanically driven by increased wind speed.  
636 For all cases, the RLWP decreases significantly from the stable phase to the dissipation phase,  
637 confirming that dissipation through fog-base lifting is linked to insufficient liquid water content in  
638 the fog layer, as suggested by the conceptual model. For case 3, the RLWP becomes negative 20  
639 min after dissipation. This delay is likely due to very rapid changes in LWP and CTH at the time of  
640 dissipation.

## 641 5. Summary and Conclusions

642 The SOFOG3D field campaign provided a unique dataset documenting thermodynamic and  
643 dynamical atmospheric circulations to further understand the processes driving fog formation and  
644 dissipation over Southeastern France. Based on an innovative instrumental synergy combining in-  
645 situ and remote sensing measurements gathered in an adiabatic fog conceptual model, this study has  
646 documented the processes favoring fog evolution. The analysis has focused on four fog case  
647 studies: two radiative and two advective-radiative fogs. For each case study, we have defined the  
648 different phases characterizing the fog life cycle, namely (i) its formation, (ii) an initial phase where  
649 the fog develops under thermally stable conditions, (iii) a transition phase towards an adiabatic fog,



650 (iv) an adiabatic phase during which the fog vertical profile is adiabatic, and (v) a dissipation phase  
651 where the fog base lifts.

652 The results showed that for both radiation fog cases, the conditions are marked by very cold  
653 atmospheric conditions associated with a continental easterly nocturnal low-level jet. For these  
654 cases, the stable fog phase develops under weak turbulence and strong surface radiative cooling and  
655 strong and deep surface temperature inversion layer. The transition phase is driven by an increase in  
656 turbulence in the fog layer. This turbulence is associated with a change in the air mass  
657 thermodynamical characteristics by advection. The adiabatic phase is observed when the turbulence  
658 ( $0.2 < \text{TKE} < 0.4 \text{ m}^2 \text{ s}^{-2}$ ) is sufficient to ensure vertical mixing in the fog layer. For these fog events,  
659 dissipation time is observed when the thermal and dynamic production of the turbulence are high  
660 ( $\text{TKE} > 0.4 \text{ m}^2 \text{ s}^{-1}$  and  $\sigma_w^2 > 0.04 \text{ m}^2 \text{ s}^{-2}$ ). For this category of fog, the adiabatic fog conceptual model  
661 estimates the dissipation time one hour before its observation.

662 The analysis on the advection-radiation case studies shows that they have the shortest life  
663 cycle linked to the low surface boundary layer stability due to the vertical mixing generated by the  
664 westerly strong wind. In this category of fog, the processes driving the stable, stable/adiabatic  
665 transition and adiabatic phases are similar to those of the radiation fog category. However, the  
666 dissipation phase is driven by night-time horizontal advection at the supersite.

667 In summary, LWP and RLWP measured during SOFOG3D present lower values than at the  
668 SIRTA site, close to the uncertainty of the measurement. The conceptual model has therefore  
669 difficulties in integrating the mixing phases in the fog layer. Further development of the model is  
670 needed to adapt it to other regions before it can be used for nowcasting prediction. Fog formation,  
671 evolution and dissipation across southern France require an analysis of the synoptic atmospheric  
672 circulation in terms of wind, cloud cover, and thermodynamical processes. Indeed, this paper  
673 highlights that fog nowcasting in this region needs in addition to the numerical weather prediction  
674 models, a cloud radar, a microwave radiometer, a wind lidar, a surface energy balance, and  
675 meteorological stations. Operationalizing these instruments would allow to improve fog  
676 nowcasting, which will reduce its socioeconomic impacts in this region.

## 677 **Appendix A: Fog conceptual model parametrization**

### 678 **A.1 Liquid water content**

679 The conceptual model for adiabatic fog has been developed at SIRTA by Toledo et al.,  
680 2021. This model is a unidimensional model inspired by previous numerical models for stratus





681 clouds (Betts, 1982, Albrecht et al., 1990; and Cermak and Bendix, 2011) (see equation 1). The  
682 basic hypothesis is to consider a well-mixed fog layer and express the increase with height of the  
683 fog liquid water content as a function of the local adiabaticity ( $\alpha(z)$ ) and the negative of the change  
684 in the saturation mixing ratio with height ( $\Gamma_{ad}(T,P)$ ), given in equation A1.

$$685 \quad \frac{dLWC(z)}{dz} = \alpha(z) \Gamma_{ad}(T, P) \quad (A1)$$

686 Where T and P are air temperature and pressure, respectively. z is the height above the  
687 surface and varies between 0 and the cloud top height (CTH). By integrating equation 1, it is  
688 important to take into account fog geometry which is different from that of the stratus cloud. For a  
689 fog, the LWC at the base is non-zero due to the presence of liquid droplets down to the ground  
690 level. This presence of droplets drives surface visibility reduction and water deposition on the soil.  
691 Thus, as indicated in equation A2, the vertical integral of the LWC(z) is a function of the variation  
692 with height of the adiabaticity,  $\Gamma_{ad}(T,P)$  and the measurement of the LWC at surface ( $LWC_0$ ). This  
693 equation shows that the LWC increases with the thickness of the fog up to the height where upward  
694 motions of moisture from the surface are constrained by downward motions of dry air from the fog  
695 top height (Walker, 2003; Cermak and Bendix, 2011). From this interface level, the LWC decreases  
696 with height and becomes zero at the fog top height (Brown and Roach, 1976; Cermak and Bendix,  
697 2011).

$$698 \quad LWC(z) = \int_{z'=0}^{z'=z} \alpha(z') \Gamma_{ad}(T, P) dz' + LWC_0 \quad (A2)$$

## 699 A.2 Liquid water path

700 The fog liquid water path (LWP) represents the total amount of liquid water present in the  
701 fog layer. It can be estimated by integrating equation A2 in height considering that the fog thickness  
702 is equivalent to the CTH (equation A3). An approximation assuming a constant adiabaticity is  
703 introduced by using the equivalent fog adiabaticity term  $\alpha_{eq}$ . This simplifies the calculation, since a  
704 complete computation would require a knowledge of the vertical profile of adiabaticity which  
705 depends on the thermodynamic properties of the fog layer. In this conceptual model, the LWC is  
706 treated as if it increased linearly with height from the surface to the CTH. At the surface level the  
707 LWC from the model and fog are the same, connecting a given LWP with surface LWC. This  
708 quantity is converted to visibility values using Gultepe et al., 2006 parametrization. Hence, the





709 conceptual model connects fog LWP with its CTH and surface visibility values, it provides an  
710 estimation of the equivalent fog adiabaticity.

$$711 \quad LWP = \frac{1}{2} \alpha_{eq} \Gamma_{ad}(T, P) CTH^2 + LWC_0 CTH \quad (A3)$$

### 712 **A.3 Critical liquid water path**

713         Considering that the fog dissipates when its liquid water path is below a certain threshold  
714 depending on the local thermodynamic atmospheric conditions. In case of dissipation by lifting the  
715 base height of the fog, Wærsted, 2018 found a deficit in LWP in the fog layer. This assertion allows  
716 defining a minimum amount of LWP necessary to maintain the horizontal visibility at surface lower  
717 or equal to 1000 m, defined as the critical liquid water path (CLWP). Thus, based on equation A3,  
718 the CLWP can be expressed in equation A4 considering a critical liquid water content at surface  
719 (LWC<sub>c</sub>). Theoretically, the LWC<sub>c</sub> is the LWC that would cause a 1000 m visibility. It is estimated  
720 from the parameterization of Gultepe et al., 2006 based on the horizontal visibility at surface.

$$721 \quad CLWP = \frac{1}{2} \alpha_{eq} \Gamma_{ad}(T, P) CTH^2 + LWC_c CTH \quad (A4)$$

722 **Data availability.** All the data used in this study are hosted by the the French national center for  
723 Atmospheric data and services AERIS in the link <https://sofog3d.aeris-data.fr/catalogue/#masthead>.  
724 Data access can be free following the conditions fixed by the SOFOG3D project.

725 **Competing interests.** The authors claim no conflict of interest for this study.

726 **Author contributions.** **Cheikh DIONE:** Conceptualization, Methodology, Investigation,  
727 Validation, Formal-analysis, Writing – original draft, Writing – review & editing, Visualization.  
728 **Martial HAEFFELIN:** Supervision, Methodology, Investigation, Formal-analysis, Writing-  
729 original draft, Writing-review & Editing, , Funding acquisition. **Jean-Charles DUPONT:**  
730 Supervision, Investigation, Editing. **Felipe TOLEDO:** Methodology, Investigation, Editing.  
731 **Frederic BURNET:** Project administration, Resources, Investigation, Editing, Funding acquisition.  
732 **Christine LAC:** Supervision, resources, Investigation, editing, Funding acquisition. **Jean-Francois**  
733 **RIBAUD:** Visualization, Investigation, Editing. **Pauline MARTINET:** Editing, Investigation,  
734 Resources, Data curation. **Guylaine CANUT:** Investigation, Editing, Data curation. **Susana**  
735 **JORQUERA:** Data curation. **Julien DELANOË:** Data curation.



736 **Acknowledgments.** The SOFOG3D field campaign was supported by METEO-FRANCE and ANR  
737 through grant AAPG 2018-CE01-0004. Data are managed by the French national center for  
738 Atmospheric data and services AERIS. The CNRM/GMEI/LISA team supported the deployment,  
739 monitoring and data processing and supplying of Wind lidar and microwave radiometer.

#### 740 **References**

- 741 1 Albrecht, B. A., Fairall, C. W., Thomson, D. W., White, A. B., Snider, J. B., and Schubert, W. H.:  
742 Surface-based remote sensing of the observed and the Adiabatic liquid water content of  
743 stratocumulus clouds, *Geophys. Res. Lett.*, 17, 89-92, <https://doi.org/10.1029/GL017i001p00089>,  
744 1990.
- 745 2 Bartok J, Bott A, Gera M.: Fog prediction for road traffic safety in a coastal desert region. *Bound-*  
746 *Layer Meteor.*, 145(3), 485-506, <https://doi.org/10.1007/s10546-012-9750-5>, 2012.
- 747 3 Bartoková I, Bott A, Bartok J, Gera M.: Fog prediction for road traffic safety in a coastal desert  
748 region: Improvement of nowcasting skills by the machine-learning approach, *Boundary-Layer*.  
749 *Meteor.*, 157, 501-516, <https://doi.org/10.1007/s10546-015-0069-x>, 2015.
- 750 4 Bell, A., Martinet, P., Caumont, O., Burnet, F., Delanoë, J., Jorquera, S., Seity, Y., and Unger, V.:  
751 An optimal estimation algorithm for the retrieval of fog and low cloud thermodynamic and micro-  
752 physical properties, *Atmos. Meas. Tech.*, 15, 5415–5438, <https://doi.org/10.5194/amt-15-5415-2022>,  
753 2022.
- 754 5 Bergot T.: Small-scale structure of journal radiation fog: a large-eddy simulation study, *Q. J. R.*  
755 *Meteor. Soc.*, 139(673):1099-1112, <https://doi.org/10.1002/qj.2051>, 2013.
- 756 6 Bergot, T., Escobar, J. and Masson, V.: Effect of small-scale surface heterogeneities and buildings  
757 on radiation fog: Large-eddy simulation study at Paris-Charles de Gaulle Airport, *Q. J. R. Meteor.*  
758 *S.*, 141(686), 285-298, <https://doi.org/10.1002/qj.2358>, 2015.
- 759 7 Betts, A. K.: Cloud Thermodynamic Models in Saturation Point Coordinates, *J. Atmos. Sci.*, 39,  
760 2182-2191, [https://doi.org/10.1175/1520-0469\(1982\)039<2182:CTMISP>2.0.CO;2](https://doi.org/10.1175/1520-0469(1982)039<2182:CTMISP>2.0.CO;2), 1982.
- 761 8 Boutle, I., Angevine, W., Bao, J.-W., Bergot, T., Bhattacharya, R., Bott, A., Ducongé, L., Forbes, R.,  
762 Goecke, T., Grell, E., Hill, A., Igel, A.L., Kudzotsa, I., Lac, C., Maronga, B., Romakkaniemi, S.,  
763 Schmidli, J., Schwenkel, J., Steeneveld, G.-J. and Vié, B.: Demistify: A large-eddy simulation (LES)  
764 and single-column model (SCM) intercomparison of radiation fog, *Atmos. Chem. Phys.*, 22(1), 319-  
765 333, <https://doi.org/10.5194/acp-22-319-2022>, 2022.
- 766 9 Braun, R. A., Dadashazar, H., MacDonald, A. B., Crosbie, E., Jonsson, H. H., Woods, R. K., Flagan,  
767 R. C., Seinfeld, J. H., and Sorooshian, A.: Cloud Adiabaticity and Its Relationship to Marine



- 768           Stratocumulus Characteristics Over the Northeast Pacific Ocean, *J. Geophys. Res. Atmos.*, 123,  
769           13790-13806, <https://doi.org/10.1029/2018JD029287>, 2018.
- 770    10 Brown, R. and Roach, W.: The physics of radiation fog: II-a numerical study, *Q. J. R. Meteor. Soc.*,  
771           102, 335-354, <https://doi.org/10.1002/qj.49710243205>, 1976.
- 772    11 Burnet, F.: SOFOG3D\_TUZAN\_CNRM\_CEILOMETER-CL51-30SEC\_L1. [Dataset], Aeris.  
773           <https://doi.org/10.25326/241>, 2021.
- 774    12 Canut, G.: SOFOG3D\_CHARBONNIERE\_CNRM\_LIDARwindcube-TKE\_L2. [Dataset]. Aeris.  
775           <https://doi.org/10.25326/323>, 2022.
- 776    13 Canut, G.: SOFOG3D\_JACHERE\_CNRM\_TURB-30MIN\_L2. [Dataset]. Aeris.  
777           <https://doi.org/10.25326/91>, 2020.
- 778    14 Canut, G.: SOFOG3D\_JACHERE\_CNRM\_TURB-30MIN\_L2. [Dataset], Aeris.  
779           <https://doi.org/10.25326/91>, 2020.
- 780    15 Cermak, J. and Bendix, J.: Detecting ground fog from space - a microphysics-based approach, *Int. J.*  
781           *Remote Sens.*, 32, 3345-3371, <https://doi.org/10.1080/01431161003747505>, 2011.
- 782    16 Crewell, S., and Löhnert, U.: Accuracy of cloud liquid water path from ground-based microwave  
783           radiometry 2. Sensor accuracy and synergy, *Radio. Sci.*, 38(3), 8042,  
784           <https://doi.org/10.1029/2002RS002634>, 2003.
- 785    17 Delanoë, J., Protat, A., Vinson, J.-P., Brett, W., Caudoux, C., Bertrand, F., Du Chatelet, J. P., Hallali,  
786           R., Barthes, L., Haeffelin, M., et al.: BASTA: A 95-GHz FMCW Doppler Radar for Cloud and Fog  
787           Studies, *J. Atmos. Ocean. Technol.* 33, 10231038: <https://doi.org/10.1175/JTECH-D-15-0104.1>,  
788           2016.
- 789    18 Dhangar, N.G., Lal, D.M., Ghude, S.D. et al.: On the Conditions for Onset and Development of Fog  
790           Over New Delhi: An Observational Study from the WiFEX, *Pure Appl. Geophys.* 178, 3727-3746,  
791           <https://doi.org/10.1007/s00024-021-02800-4>, 2021.
- 792    19 Dias Neto, J., Nuijens, L., Unal, C., and Knoop, S.: Combined wind lidar and cloud radar for high-  
793           resolution wind profiling, *Earth Syst. Sci. Data*, 15, 769-789, [https://doi.org/10.5194/essd-15-769-](https://doi.org/10.5194/essd-15-769-2023)  
794           [2023](https://doi.org/10.5194/essd-15-769-2023), 2023.
- 795    20 Ducongé, L., C. Lac, B. Vié, T. Bergot, and J. D., Price, Fog in heterogeneous environments : The  
796           relative importance of local and non local processes on radiative advective fog formation, *Q. J. R.*  
797           *Meteor. Soc.*, 146, 2522-2546, <https://doi.org/10.1002/qj.3783>, 2020.
- 798    21 Dupont, J.-C., Haeffelin, M., Protat, A., Bouniol, D., Boyouk, N., and Morille, Y.: Stratus-fog  
799           formation and dissipation: a 6-day case study, *Bound.-Layer. Meteorol.*, 143, 207-225,  
800           <https://doi.org/10.1007/s10546-012-9699-4>, 2012.
- 801    22 Fathalli, M., Lac, C., Burnet, F., Vié B.: Formation of fog due to stratus lowering: An observational  
802           and modeling case study, *Q. J. R. Meteor. Soc.*, <https://doi.org/10.1002/qj.4304>, 2022.



- 803 23 Fernando, H. J., Gultepe, I., Dorman, C., Pardyjak, E., Wang, Q., Hoch, S. W., et al.: C-FOG: life of  
804 coastal fog, *Bull Am Meteor Soc* 102(2):E244–E272. <https://doi.org/10.1175/BAMS-D-19-0070.1>,  
805 2021.
- 806 24 Foken, T., Göckede, M., Mauder, M., Mahrt, L., Amiro, B. D., and Munger, J. W.: Post-field data  
807 quality control, in: *Handbook of Micrometeorology: A Guide for Surface Flux Measurement and*  
808 *Analysis*, edited by: Lee, X., Massman, W. J., and Law, B., Kluwer, Dordrecht, 181-208,  
809 <https://doi.org/10.1007/1-4020-2265-4>, 2004.
- 810 25 Ghude, S. D., et al.: WiFEX: Walk into the warm fog over Indo Gangetic Plain region. *Bulletin of*  
811 *the American Meteorological Society.*, <https://doi.org/10.1175/BAMS-D-21-0197.1>, 2023.
- 812 26 Huang, H. B., Chen, C. Y.: Climatological aspects of dense fog at Urumqi Diwopu International  
813 Airport and its impacts on flight on-time performance. *Nat Hazards* 81(2):1091-1106,  
814 <https://doi.org/10.1007/s11069-015-2121-z>, 2016.
- 815 27 Haeffelin, M., Bergot, T., Elias, T., Tardif, R., Carrer, D., Chazette, P., Colomb, M., Drobinski, P.,  
816 Dupont, E., Dupont, J.-C., Gomes, L., Musson-Genon, L., Pietras, C., Plana-Fattori, A., Protat, A.,  
817 Rangognio, J., Raut, J.-C., Rmy, S., Richard, D., Sciare, J. and Zhang, X.: Parisfog: shedding new  
818 light on fog physical processes. *Bulletin of the American Meteorological Society.*, 91(6), 767-783,  
819 <https://doi.org/10.1175/2009BAMS2671.1>, 2010.
- 820 28 Koračin, D., Dorman, C. E., Lewis, J. M., Hudson, J. G., Wilcox, E. M., Torregrosa A.: Marine fog:  
821 a review, *Atmos. Res.*, 143:142-175, <https://doi.org/10.1016/j.atmosres.2013.12.012>, 2014.
- 822 29 Kumer, V. M., Reuder, J., Dorninger, M., Zauner, R., Grubišić, V.: Turbulent kinetic energy  
823 estimates from profiling wind LiDAR measurements and their potential for wind energy  
824 applications, *Renew Energy.*, 99, 898-910, <https://doi.org/10.1016/j.renene.2016.07.014>, 2016.
- 825 30 Liao, H., Jing, H., Ma, C., Tao, Q., Li, Z.: Field measurement study on turbulence field by wind  
826 tower and Windcube Lidar in mountain valley, *Journal of Wind Engineering and Industrial*  
827 *Aerodynamics.*, 197, 104090, ISSN 0167-6105, <https://doi.org/10.1016/j.jweia.2019.104090>, 2020.
- 828 31 Liu, D. Y., Niu S. J., Yang, J., Zhao, L. J., Lü, J. J., Lu, C. S.: Summary of a 4-year fog field study in  
829 northern Nanjing, Part 1: fog boundary layer, *Pure. Appl. Geophys.*, 169(5-6), 809-819,  
830 <https://doi.org/10.1007/s00024-011-0343-x>, 2012.
- 831 32 Liu, D. Y., Yan, W. L., Yang, J., Pu, M. J., Niu, S. J., Li, Z. H.: A study of the physical processes of  
832 an advection fog boundary layer, *Boundary- Layer. Meteor.*, 158, 125-138,  
833 <https://doi.org/10.1007/s10546-015-0076-y>, 2016.
- 834 33 Maalick, Z., Kühn, T., Korhonen, H., Kokkola, H., Laaksonen, A. and Romakkaniemi, S.: Effect of  
835 aerosol concentration and absorbing aerosol on the radiation fog life cycle, *Atmospheric*  
836 *Environment*, 133, 26-33, <https://doi.org/10.1016/j.atmosenv.2016.03.018>, 2016.



- 837 34 Marke, T., Ebell, K., Löhnert, U., Turner, D. D.: Statistical retrieval of thin liquid cloud  
838 microphysical properties using ground-based infrared and microwave observations, *J. Geophys. Res.*  
839 *Atmos.*, 121(24):14-558, <https://doi.org/10.1002/2016JD025667>, 2016.
- 840 35 Martinet, P., Unger, V., Burnet, F. *et al.*: A dataset of temperature, humidity, and liquid water path  
841 retrievals from a network of ground-based microwave radiometers dedicated to fog investigation,  
842 *Bull. of Atmos. Sci. Technol.*, **3**, 6, <https://doi.org/10.1007/s42865-022-00049-w>, 2022.
- 843 36 Martinet, P. (2021). SOFOG3D\_CHARBONNIERE\_CNRM\_MWR-HATPRO-LWP\_L2. [Dataset].  
844 *Aeris*. <https://doi.org/10.25326/207>
- 845 37 Mauder, M., Cuntz, M., Drüe, C., Graf, A., Rebmann, C., Schmid, H. P., Schmidt, M., and  
846 Steinbrecher, R.: A strategy for quality and uncertainty assessment of long-term eddy-covariance  
847 measurements, *Agr. Forest Meteorol.*, **169**, 122-135,  
848 <https://doi.org/10.1016/j.agrformet.2012.09.006>, 2013.
- 849 38 Mazoyer, M., Lac, C., Thouron, O., Bergot, T., Masson, V., and Musson-Genon, L.: Large eddy  
850 simulation of radiation fog: impact of dynamics on the fog life cycle, *Atmos. Chem. Phys.*, **17**,  
851 13017-13035, <https://doi.org/10.5194/acp-17-13017-2017>, 2017.
- 852 39 Nakanishi M.: Large-Eddy simulation of radiation fog, *Bound-Layer Meteorol.*, **94**, 461-493,  
853 <https://doi.org/10.1023/A:1002490423389>, 2000.
- 854 40 Niu, S., Lu, C., Yu, H., Zhao, L., and Lü, L.: Fog research in China: an overview, *Adv. Atmos.*  
855 *Sci.*, **27**(3), 639-662, <https://doi.org/10.1007/s00376-009-8174-8>, 2010a.
- 856 41 Niu, S., Lu, C., Zhao, J., Lu, J., and Yang, J.: Analysis of the microphysical structure of heavy fog  
857 using a droplet spectrometer: a case study, *Adv. Atmos. Sci.*, **27**(6), 1259-1275,  
858 <https://doi.org/10.1007/s00376-010-8192-6>, 2010b.
- 859 42 Pauli, E., Cermak, J., Andersen, H.: A satellite-based climatology of fog and low stratus formation  
860 and dissipation times in central Europe, *Q. J. Roy. Meteorol. Soc.*, **148**, 1439-1454,  
861 <https://doi.org/10.1002/qj.4272>, 2022.
- 862 43 Philip, A., Bergot, T., Bouteloup, Y., and Bouysse, F.: The impact of vertical resolution on fog  
863 forecasting in the kilometric-scale model Arome: a case study and statistics, *Weather Forecast.*, **31**,  
864 1655-1671, <https://doi.org/10.1175/WAF-D-16-0074.1>, 2016.
- 865 44 Pithani, P., Ghude, S.D., Jenamani, R.K., Biswas, M., Naidu, C.V., Debnath, S., Kulkarni, R.,  
866 Dhangar, N.G., Jena, C., Hazra, A., Phani, R., Mukhopadhyay, P., Prabhakaran, T., Nanjundiah,  
867 R.S., Rajeevan, M.: Real-time Forecast Of Dense Fog Events Over Delhi: The Performance Of the  
868 WRF Model During WiFEX Field Campaign. *Weather and Forecasting*, **35**(2), 739-756,  
869 <https://doi.org/10.1175/waf-d-19-0104.1>, 2020.
- 870 45 Price, J. D.: On the formation and development of radiation fog: an observational study. *Bound-*  
871 *Layer Meteorol.*, **172**, 167-197, <https://doi.org/10.1007/s10546-019-00444-5>, 2019.



- 872 46 Price, J. D., Lane, S., Boutle, I. A., Smith, D. K. E., Bergot, T., Lac, C., Duconge, L., McGregor, J.,  
873 Kerr-Munslow, A., Pickering, M., and Clark, R.: LANFEX: a field and modeling study to improve  
874 our understanding and forecasting of radiation fog, *Bull. Amer. Meteor. Soc.*, 99, 2061-2077,  
875 <https://doi.org/10.1175/BAMS-D-16-0299.1>, 2018.
- 876 47 Price, J.: Radiation Fog. Part I: Observations of Stability and Drop Size Distributions, *Boundary-*  
877 *Layer Meteorol.*, 139, 167-191, <https://doi.org/10.1007/s10546-010-9580-2>, 2011.
- 878 48 Price, J., Porson, A., and Lock, A.: An observational case study of persistent fog and comparison  
879 with an ensemble forecast model, *Boundary-Layer Meteorol.*, 155, 301-327,  
880 <https://doi.org/10.1007/s10546-014-9995-2>, 2015.
- 881 49 Roach, W.: Back to basics: Fog: Part 2 - the formation and dissipation of land fog, *Weather.*, 50(1),  
882 7-11, 1995.
- 883 50 Román-Cascón, C., Steeneveld, G. J., Yagüe, C., Sastre, M., Arrillaga, J. A., and Maqueda, G.:  
884 Forecasting radiation fog at climatologically contrasting sites: Evaluation of statistical methods and  
885 WRF. *Q. J. R. Meteorol. Soc.*, 142(695), 1048-1063, <https://doi.org/10.1002/qj.2708>, 2016.
- 886 51 Ryznar, E.: Advection-radiation fog near Lake Michigan, *Atmos. Environ.* 11, 427-430,  
887 [https://doi.org/10.1016/0004-6981\(77\)90004-X](https://doi.org/10.1016/0004-6981(77)90004-X), 1977.
- 888 52 Steeneveld, G. J., Ronda, R. J., and Holtslag, A. A. M.: The challenge of forecasting the onset and  
889 development of radiation fog using mesoscale atmospheric models, *Boundary-Layer Meteorology*,  
890 154(2), 265-289, <https://doi.org/10.1007/s10546-014-9973-8>, 2015.
- 891 53 Tardif, R. and Rasmussen, R. M.: Event-based climatology and typology of fog in the New York  
892 City region, *J. Appl. Meteorol. Clim.*, 46, 1141-1168, <https://doi.org/10.1175/JAM2516.1>, 2007.
- 893 54 Ju, T., Wu, B., Zhang, H., Liu, J., 2020.: Characteristics of turbulence and dissipation mechanism in  
894 a polluted advection-radiation fog life cycle in Tianjin, *Meteorology and Atmospheric Physics.*,  
895 <https://doi.org/10.1007/s00703-020-00764-z>, 2020.
- 896 55 Toledo, F., Haefelin, M., Wærsted, E., and Dupont, J.-C.: A new conceptual model for adiabatic  
897 fog, *Atmos. Chem. Phys.*, 21, 13099-13117, <https://doi.org/10.5194/acp-21-13099-2021>, 2021.
- 898 56 Felipe Toledo Bittner. Improvement of cloud radar products for fog surveillance networks : fog life  
899 cycle analyses and calibration methodologies, Ph.D. Thesis, Institut Polytechnique de Paris, France,  
900 (NNT : 2021IPPAX029). (tel-03298445), 2021.
- 901 57 Toledo, F., Delanoë, J., Haefelin, M., Dupont, J.-C., Jorquera, S., and Le Gac, C.: Absolute  
902 calibration method for frequency-modulated continuous wave (FMCW) cloud radars based on corner  
903 reflectors, *Atmos. Meas. Tech.*, 13, 6853-6875, <https://doi.org/10.5194/amt-13-6853-2020>, 2020.



- 904 58 Wærsted, E. G., Haeffelin, M., Steeneveld, G.-J., and Dupont, J.-C.: Understanding the dissipation of  
905 continental fog by analysing the LWP budget using idealized LES and in situ observations, Q. J.  
906 Roy. Meteor. Soc., 145, 784-804, <https://doi.org/10.1002/qj.3465>, 2019.
- 907 59 Wærsted, E. G. Description of physical processes driving the life cycle of radiation fog and fog-  
908 stratus transitions based on conceptual models, Ph.D. Thesis, Paris Saclay, 2018.
- 909 60 Wærsted, E. G., Haeffelin, M., Dupont, J.-C., Delanoë, J., and Dubuisson, P.: Radiation in fog:  
910 quantification of the impact on fog liquid water based on ground-based remote sensing, Atmos.  
911 Chem. Phys., 17, 10811–10835, <https://doi.org/10.5194/acp-17-10811-2017>, 2017.
- 912 61 Walker, M.: The science of weather: Radiation fog and steam fog, Weather, 58, 196-197,  
913 <https://doi.org/10.1256/wea.49.02>, 2003.
- 914 62 Zhou, B., and Ferrier, B. S.: Asymptotic analysis of equilibrium in radiation fog. Journal of Applied  
915 Meteorology and Climatology, 47, 1704-1722. <https://doi.org/10.1175/2007JAMC1685.1>, 2008.



916 **List of tables**

917 **Table 1 :** Case study number, fog onsets, type of fog formation, fog dissipation times, fog duration  
918 and type of fog dissipation for the four documented case studies. Time is in UTC. Dates are in the  
919 format “dd/mm/yyyy”. “dd” indicates the day, “mm” the month, and “yyyy” the year.

920 **Table 2 :** Summary of fog features at the supersite during the five defined phases during its  
921 evolution for each case study. The formation, dissipation times are estimated using the visibility (m)  
922 from the Scatterometer. The transition from stable to adiabatic fog is defined using temperature  
923 from the microwave radiometer. The cooling rate ( $dT/dt$ ), wind speed (WS), and wind direction  
924 (WD) are derived from the meteorological station. Sensible heat flux (SHF), turbulent kinetic  
925 energy (TKE) and the vertical velocity variance ( $\sigma_w^2$ ) at 3 m a.g.l are derived from the flux station.  
926 The liquid water path (LWP) is estimated from the MWR. The fog reservoir of liquid weather path  
927 (RLWP) and the equivalent adiabaticity of closure  $\alpha_{eq}^{closure}$  parameter are computed by the  
928 conceptual model. Fog top height (FTH) and middle and high cloud base and top heights are  
929 derived from the radar reflectivity from Basta cloud radar.”-” indicates that the variables are not  
930 measurable or calculable.





931 **List of figures**

932 **Figure 1:** In a), the geographical map of the study area of the SOFOG3D field campaign including  
933 the five instrumented sites (Agen, Bergerac, Biscarrosse, Mont-de-Marsan, and Saint-Symphorien)  
934 where a microwave radiometer was installed. Blue lines indicate the rivers. The cities are indicated  
935 in black dots. The most instrumented domain around the supersite is indicated in a) by the red  
936 rectangle. In b), the orography of a 100 x 100 km<sup>2</sup> domain centered on Charbonnière which includes  
937 locations of four of the meteorological stations installed around the supersite used in this study.  
938 Orography data are from the National Aeronautics and Spatial Administration (NASA) shuttle radar  
939 topography mission (SRTM) (90 m of resolution).

940 **Figure 2:** **Figure 2:** (a) Scatter plot of the equivalent adiabaticity by closure versus the CTH and  
941 LWP at the supersite. b) Boxplot of the equivalent adiabaticity by closure versus the different LWP  
942 ranges from the MWR. In b), numbers at the figure top indicate total values included in each  
943 boxplot and computed between 2 hours before and after the fog. Horizontal dashed line indicates  
944 the threshold of the equivalent adiabaticity from closure defining the transition from stable to  
945 adiabatic fog.

946 **Figure 3:** In (a-b) time-height cross-section from surface up to 600 and 12000 m, respectively of  
947 radar reflectivity from Basta (shaded) radar, time evolution of the cloud top height from Basta (red  
948 line), and the cloud base height from the Celiometer (CL51) (green line). Time evolution of (c)  
949 surface visibility, (d) 10 m wind speed, (e) 2 m air temperature, and (f) 10 m wind direction  
950 observed on the 28-29 December 2019 (case study 1, IOP 5) at the five meteorological stations (in  
951 red, black, blue, green, and pink lines for Moustey (1 m a.g.l), Charbonnière (3 m a.g.l), Cape Sud  
952 (3 m a.g.l), Tuzan (3 m a.g.l), and Noailan (1 m a.g.l), respectively) deployed around the supersite.  
953 Note that wind was not collected at Tuzan. In (c), the visibility measured at Moustey was  
954 interrupted by technical issues. Vertical black dashed lines indicate fog formation (left) and  
955 dissipation (right) times. Green dashed lines show the transition time from stable fog to adiabatic  
956 fog (fog mature phase). Red dashed line indicates the sunrise.

957 **Figure 4:** Evolution of fog macrophysical characteristics observed on the 28-29 December 2019  
958 (case study 1, IOP 5) at Charbonnière. In (a-b) vertical profiles of air temperature from the Hatpro  
959 microwave radiometer (MWR) and radar reflectivity from Basta radar, respectively. In (c) time-



960 height cross-section of air temperature from the MWR (shaded), time evolution of inversion top  
961 height (ITH) (open gray circles), inversion base height (IBH) (open gray squares), cloud top height  
962 (CTH) from the cloud radar (open black squares), and the cloud base height (CBH) from the  
963 Celiometer (open black circles). In (d) wind speed (shaded) and direction (arrows) from the  
964 WindCube. Arrows in (d) indicate only the direction of the horizontal flow. Time evolution of (e)  
965 air temperature at 3 m a.g.l from the meteorological station (red line) and equivalent adiabaticity of  
966 closure from the fog conceptual model (blue line), (f) the mean of the turbulent kinetic energy  
967 (TKE) in the layer 40 – 220 m for the WindCube (black line) and the TKE (blue line) and vertical  
968 velocity variance (red line) at 3 m a.g.l from the flux station at Charbonnière, (g) the LWP estimate  
969 from the MWR (blue line), the RLWP from the fog conceptual model (red line), and (h) sensible  
970 heat fluxes (SHF) (red and blue lines, respectively) from the flux station. Vertical black dashed lines  
971 indicate fog formation and dissipation times. Green dashed lines indicate the transition period (fog  
972 mature phase) from stable to adiabatic fog. The red dashed line indicates sunrise.

973 **Figure 5:** As in Figure 3 but for the 5-6 January 2020 (case study 2, IOP 6). In (c), only  
974 Charbonnière and Noaillan have valid data. In (c), the visibility measured at Moustey, Tuzan and  
975 Cape Sud were interrupted by technical issues.

976 **Figure 6:** As in Figure 4 but for the 5-6 January 2020 (case study 2, IOP6).

977 **Figure 7:** As in Figure 3 but for the 8-9 February 2020 (case study 3, IOP 11).

978 **Figure 8:** As in Figure 4 but for the 8-9 February 2020 (case study 3, IOP 11).

979 **Figure 9:** As in Figure 3 but for the 7-8 March 2020 (case study 4, IOP 14).

980 **Figure 10:** As in Figure 4 but for the 7-8 March 2020 (case study 4, IOP 14). The LWP, RLWP,  
981 and  $\alpha_{\text{eq}}^{\text{closure}}$  are disrupted between 00:30 and 02:30 UTC because the LWP estimated by the MWR  
982 take into account the liquid water in the advected stratus.

983 **Figure 11:** Vertical profiles of air temperature and radar reflectivity put together for each fog case  
984 study: (a) for case study 1, (b) case study 2, (c) case study 3 and (d) case study 4. Line and shaded

<https://doi.org/10.5194/egusphere-2023-1224>

Preprint. Discussion started: 9 June 2023

© Author(s) 2023. CC BY 4.0 License.

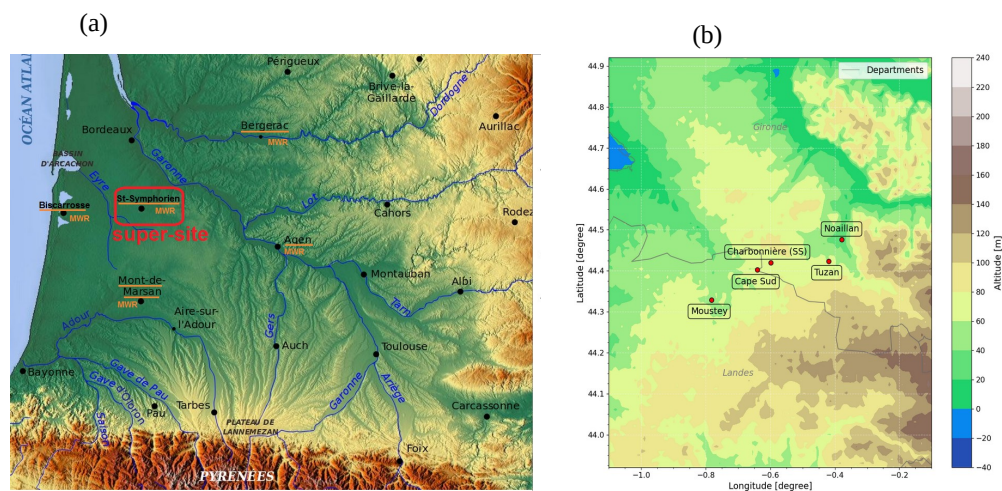


985 area indicate the mean and standard deviation of air temperature and radar reflectivity during each  
986 fog phase.

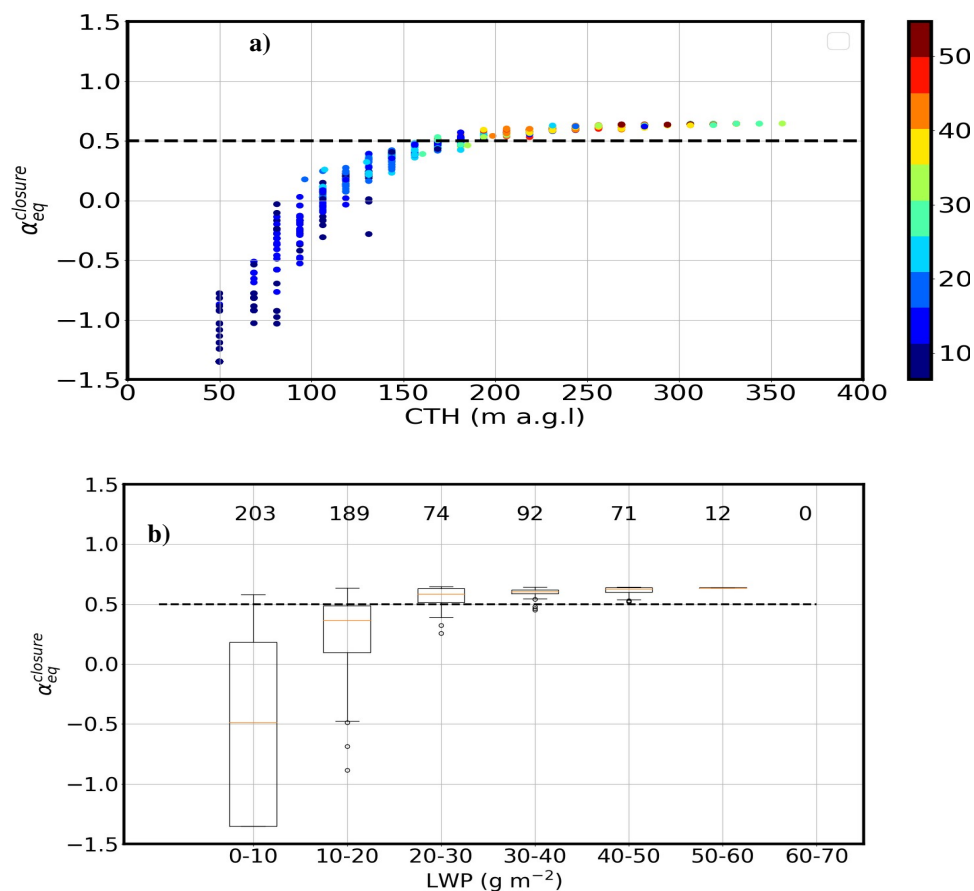


987 **Table 2** : Summary of fog features at the supersite, during the five defined phases during its evolution for each case  
 988 study. The formation, dissipation times are estimated using the visibility (m) from Scatterometer. The cooling rate  
 989 ( $dT/dt$ ), wind speed (WS) and wind direction (WD) are derived from the meteorological station. Sensible heat flux  
 990 (SHF), turbulent kinetic energy (TKE), and the vertical velocity variance ( $\sigma_w^2$ ) at 3 m a.g.l are derived from the flux  
 991 station. The liquid water path (LWP) is estimated from the MWR. The fog reservoir of liquid weather path (RLWP) and  
 992 the equivalent adiabaticity of closure  $\alpha_{eq}^{closure}$  parameter are computed by the conceptual model. Fog top height (FTH)  
 993 and middle and high cloud base and top heights are derived from the radar reflectivity from Basta cloud radar.”-”  
 994 indicates that the variables are not measurable or calculable.

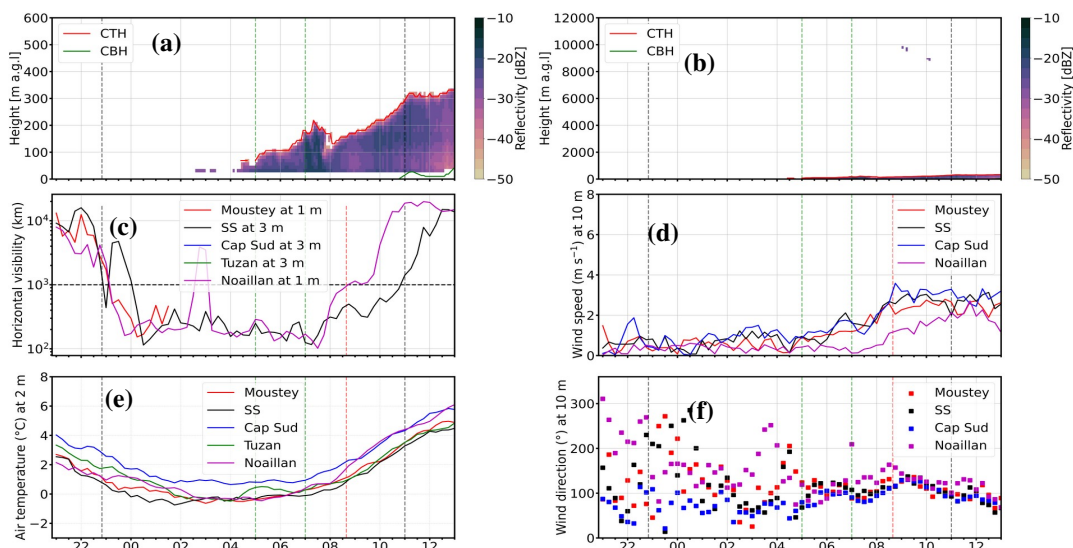
Case study number	Phase names	Time range	Duration (h:min)	Visibility (m)	$dT/dt$ ( $^{\circ}C h^{-1}$ )	$\alpha_{eq}^{closure}$ $g m^{-3}$	LWP (g $m^{-2}$ )	RLWP max (g $m^{-2}$ )	FTH (m a.g.l)	WS (m $s^{-1}$ )	WD ( $^{\circ}$ )	TKE (m $^2 s^{-2}$ )	$\sigma_w^2$ (m $^2 s^{-2}$ )	SHF (W $m^{-2}$ )	Cloud above fog (m a.g.l)
1 (IOP5)	Pre-fog phase	[20:50 - 22:50]	2:00	9962	-0.9	-	0	-	-	0.61	61	0.18	0.002	-0.23	clear
	Stable	[22:50 - 05:00]	6:10	736	-0.18	-1.3	2.18	-	51	0.7	84	0.12	0.01	-1.16	clear
	Transition stable/adiabatic	[05:00 - 07:00]	2:00	173 – 262	0.08	-0.8 – 0.4	7 – 28	8 – 15	68 – 181	0.5 – 2.1	68 – 112	0.07 – 0.17	0.02 – 0.03	2.3 – 8.8	clear
	Adiabatic	[07:00 - 11:00]	4:00	370	0.77	0.5	26.16	6.38	185	2.4	116	0.28	0.04	12.9	[8000 - 10000]
	Dissipation	[10:30 - 11:30]	1:00	1549	1.1	0.63	43.34	-11.39	288	2.6	94	0.46	0.06	22.02	clear
2 (IOP6)	Pre-fog	[18:40 - 20:40]	2:00	15566	-0.7	-	0	-	-	0.2	195	0.06	0.003	-0.17	clear
	Stable	[20:40 - 00:00]	3:20	242	-0.13	-0.69	1.66	-	71	1	183	0.09	0.009	0.28	clear
	Transition stable/adiabatic	[00:00 - 02:00]	2:00	219 – 291	-0.007	-0.2 – 0.45	0.3 – 17	-0.23 – 3.8	81 – 168	1.6 – 2.6	149 – 147	0.35 – 0.25	0.02 – 0.04	3.7 – 11	clear
	Adiabatic	[02:00 - 08:40]	6:40	450	0.17	0.51	22.14	1.51	191	2.2	110	0.27	0.04	6.62	clear
	Dissipation	[08:10 - 09:10]	1:00	944	0.43	0.53	11.62	-7.63	187	2.5	136	0.33	0.048	14.02	[250 - 1000]
3 (IOP11)	Pre-fog	[18:40 - 20:40]	2:00	13239	-1.03	-	0	-	-	1.3	242	0.03	0.011	-5.5	rain
	Stable	[20:40 - 23:00]	2:20	243	-1.2	-0.69	6.10	-	77	1	220	0.06	0.002	-1.7	clear
	Transition stable/adiabatic	[23:00 - 02:30]	3:30	134 – 260	-0.08	-1.35 – 0.4	5 – 19.8	7.7 – 6	50 – 156	1.8 – 0.4	144 – 78	0.07 – 0.04	0.006 – 0.004	-1.9 – -0.2	clear
	Adiabatic	[02:30 - 03:40]	1:10	271	0.81	0.54	30.70	3.45	204	1	120	0.08	0.008	-0.49	clear
	Dissipation	[03:10 - 04:10]	1:00	1445	1.34	0.6	41.90	2.03	235	3.6	143	0.42	0.07	-3.02	clear
4 (IOP14)	Pre-fog	[19:20 - 21:20]	2:00	14088	-0.47	-	0	-	-	1.1	233	0.06	0.002	-1.17	[5000 - 6000] [8000 - 10000]
	Stable	[21:20 - 23:30]	2:10	230	-0.88	-0.46	11.34	-	81	1.2	177	0.09	0.012	-3.26	clear
	Transition stable/adiabatic	[23:30 - 01:00]	1:30	240 – 253	0.12	-0.17 – 0.64	10.9 – 59.2	10 – -	106 – 209	1.6 – 2.7	141 – 184	0.08 – 0.32	0.01 – 0.05	-1.6 – 2.7	clear
	Adiabatic	[00:20 - 04:00]	3:40	372	0.47	0.59	43.02	8.10	292	2	179	0.22	0.03	1.2	[250 - 500]
	Dissipation	[03:30 - 04:30]	1:00	1160	-0.14	0.60	39.74	-2.32	240	2.7	174	0.27	0.04	0.82	clear



995 **Figure 1** : In a), the orography of the study area of the SOFOG3D field campaign including the five  
996 instrumented sites (Agen, Bergerac, Biscarrosse, Mont-de-Marsan, and Saint-Symphorien) where a  
997 microwave radiometer was installed. Blue lines indicate the rivers. The cities are indicated in black  
998 dots. The most instrumented domain around the supersite is indicated in a) by the red rectangle. In  
999 b), the orography of a 100 x 100 km<sup>2</sup> domain centered on Charbonnière which includes locations of  
1000 four of the meteorological stations installed around the supersite and used in this study. Orography  
1001 data are from the National Aeronautics and Spatial Administration (NASA) shuttle radar  
1002 topography mission (SRTM) (90 m of resolution).

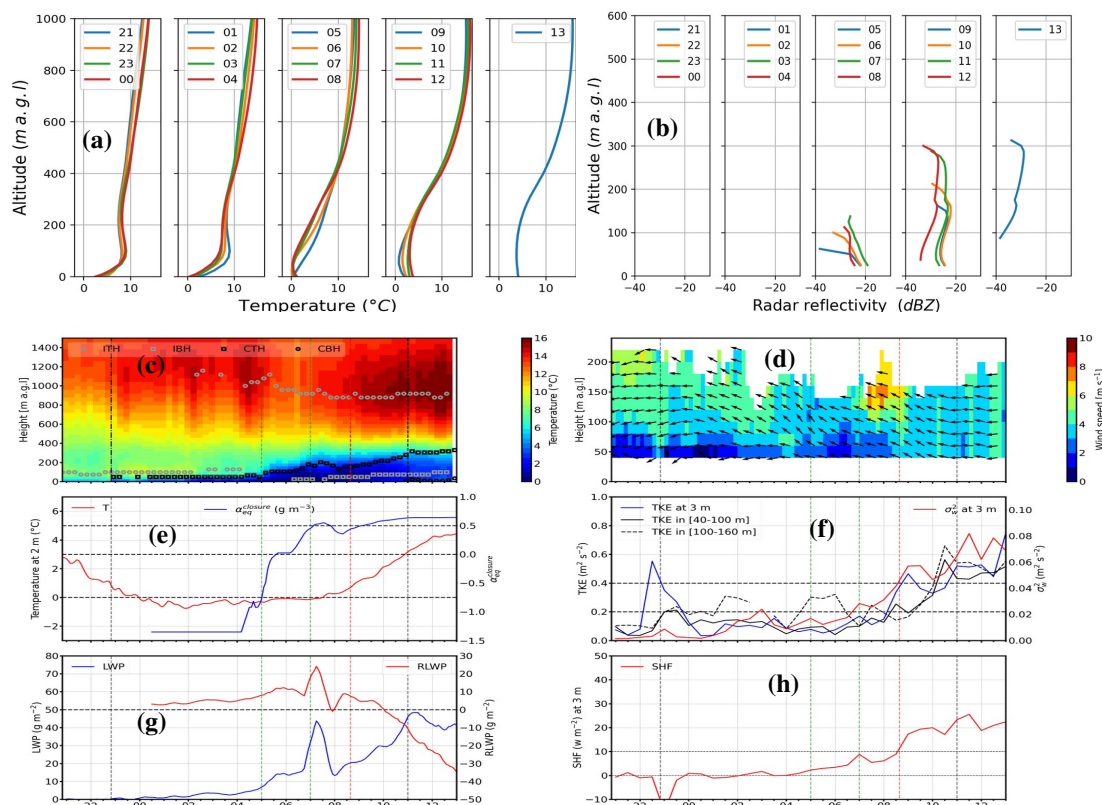


1003 **Figure 2:** In (a) Scatter plot of the equivalent adiabaticity by closure versus the CTH and LWP  
 1004 (colored circles) at the supersite. b) Boxplot of the equivalent adiabaticity by closure versus the  
 1005 different LWP ranges from the MWR. In b), numbers at the figure top indicate total values included  
 1006 in each boxplot and computed between 2 hours before and after the fog. Horizontal dashed line  
 1007 indicates the threshold of the equivalent adiabaticity from closure defining the transition from stable  
 1008 to adiabatic fog.



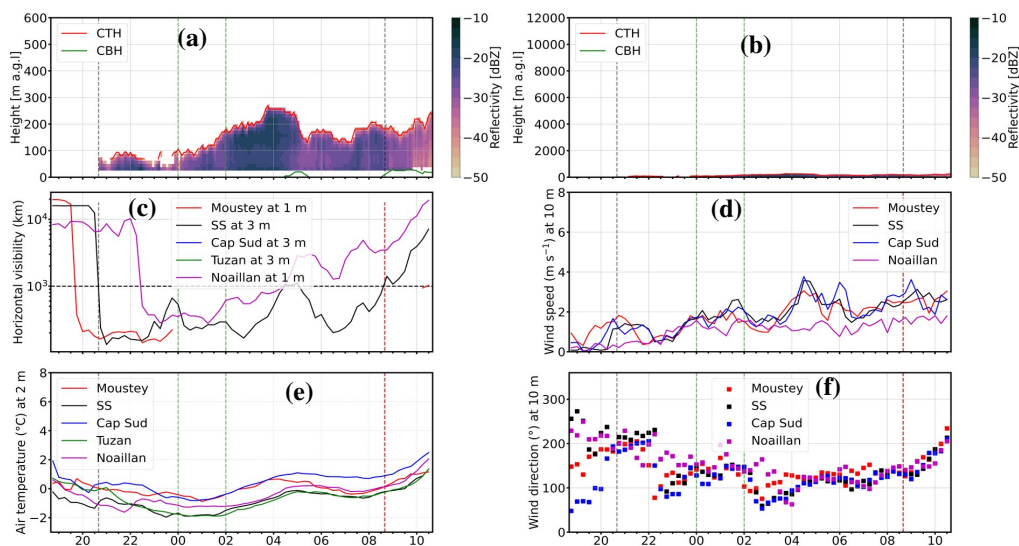
1009 **Figure 3:** In (a-b) time-height cross-section from surface up to 600 and 12000 m, respectively of  
 1010 radar reflectivity from Basta (shaded) radar, time evolution of the cloud top height from Basta (red  
 1011 line), and the cloud base height from the Celiometer (CL51) (green line). Time evolution of (c)  
 1012 surface visibility, (d) 10 m wind speed, (e) 2 m air temperature, and (f) 10 m wind direction  
 1013 observed on the 28-29 December 2019 (case study 1, IOP 5) at the five meteorological stations (in  
 1014 red, black, blue, green, and pink lines for Moustey (1 m a.g.l), Charbonnière (3 m a.g.l), Cape Sud  
 1015 (3 m a.g.l), Tuzan (3 m a.g.l), and Noaillan (1 m a.g.l), respectively) deployed around the supersite.  
 1016 Note that wind was not collected at Tuzan. In (c), the visibility measured at Moustey was  
 1017 interrupted by technical issues. Vertical black dashed lines indicate fog formation (left) and  
 1018 dissipation (right) times. Green dashed lines show the transition time from stable fog to adiabatic  
 1019 fog (fog mature phase). Red dashed line indicates the sunrise.



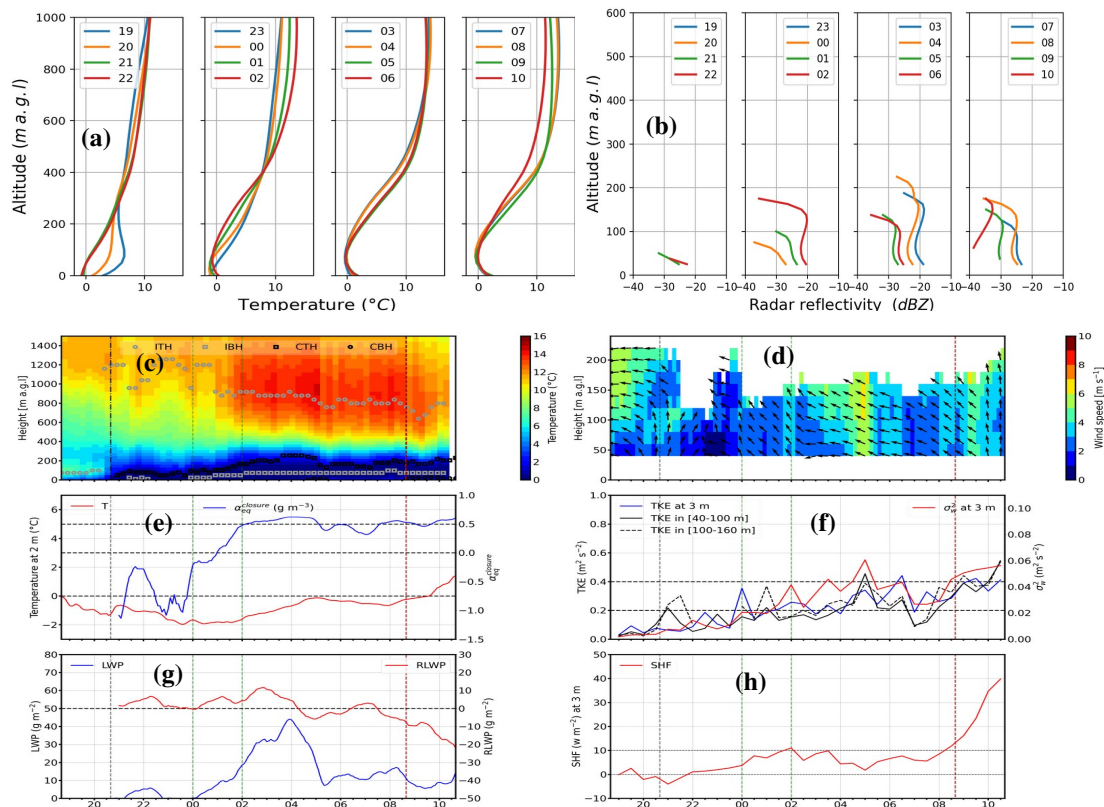


1020 **Figure 4:** Evolution of fog macrophysical characteristics observed on the 28-29 December 2019 (case study  
 1021 1, IOP 5) at Charbonnière. In (a-b) vertical profiles of air temperature from the Hatpro microwave radiometer  
 1022 (MWR) and radar reflectivity from Basta radar, respectively. In (c) time-height cross-section of air  
 1023 temperature from the MWR (shaded), time evolution of inversion top height (ITH) (open gray squares),  
 1024 inversion base height (IBH) (open gray squares), cloud top height (CTH) from the cloud radar (open black  
 1025 squares), and the cloud base height (CBH) from the Celiometer (open black circles). In (d) wind speed  
 1026 (shaded) and direction (arrows) from the WindCube. Arrows in (d) indicate only the direction of the  
 1027 horizontal flow. Time evolution of (e) air temperature at 3 m a.g.l from the meteorological station (red line)  
 1028 and equivalent adiabaticity of closure from the fog conceptual model (blue line), (f) the mean of the turbulent  
 1029 kinetic energy (TKE) in the layer 40 – 220 m for the WindCube (black line) and the TKE (blue line) and  
 1030 vertical velocity variance (red line) at 3 m a.g.l from the flux station at Charbonnière, (g) the LWP estimate  
 1031 from the MWR (blue line), the RLWP from the fog conceptual model (red line), and (h) sensible heat fluxes  
 1032 (SHF) (red and blue lines, respectively) from the flux station. Vertical black dashed lines indicate fog  
 1033 formation and dissipation times. Green dashed lines indicate the transition period (fog mature phase) from  
 1034 stable to adiabatic fog. The red dashed line indicates sunrise.

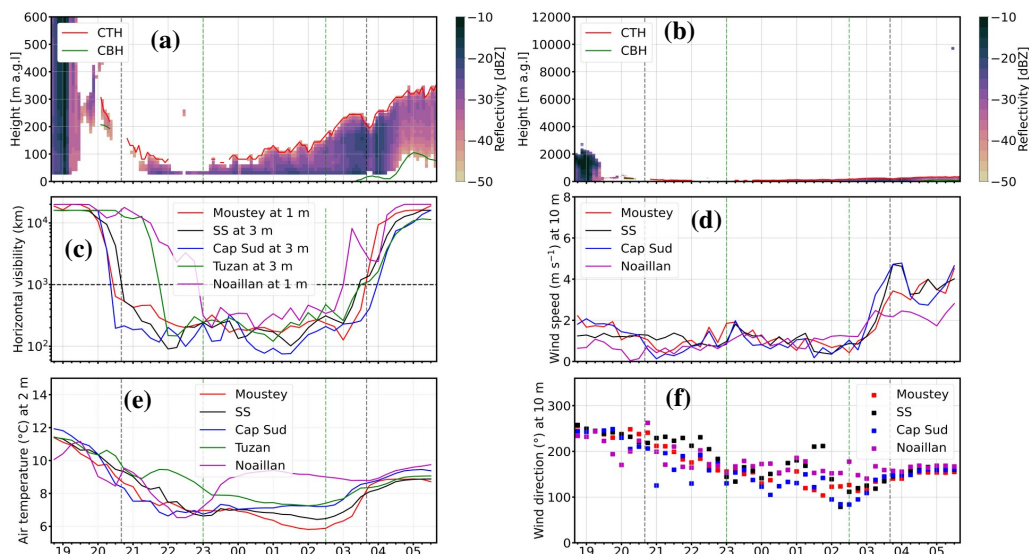




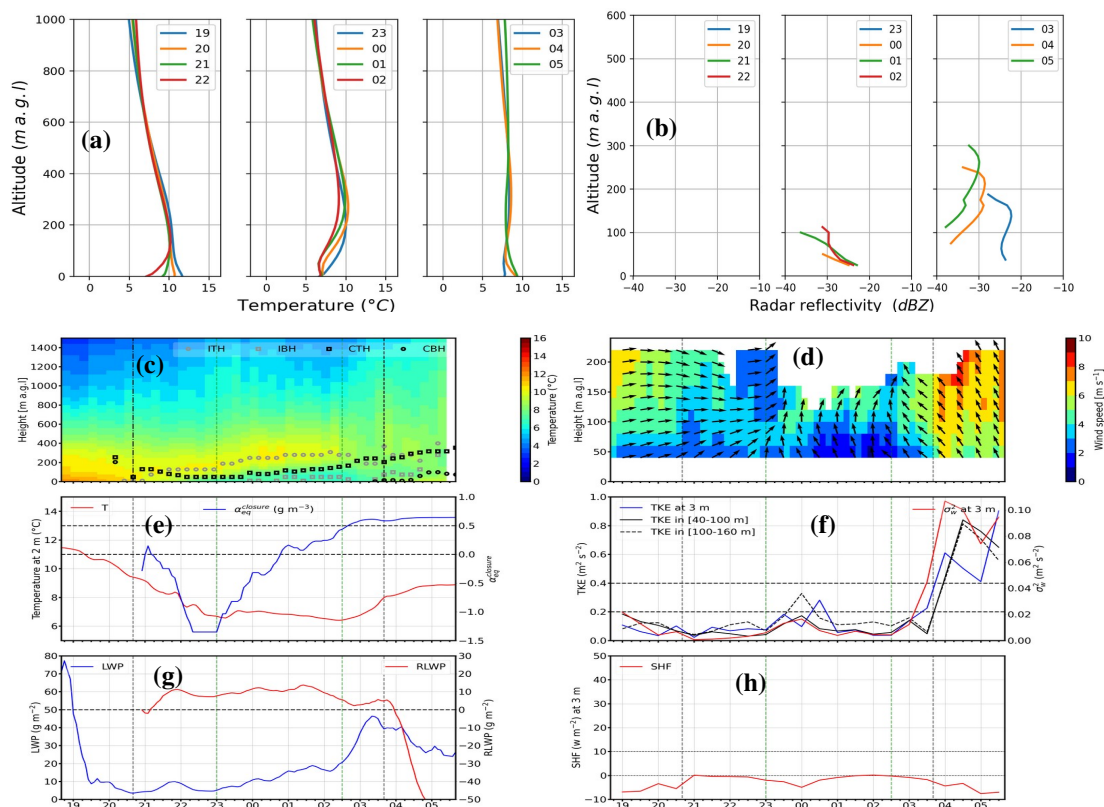
1035 **Figure 5:** As in Figure 3 but for the 5-6 January 2020 (case study 2, IOP 6). In (c), only  
 1036 Charbonnière and Noaillan have valid data. In (c), the visibility measured at Moustey, Tuzan and  
 1037 Cape Sud were interrupted by technical issues.



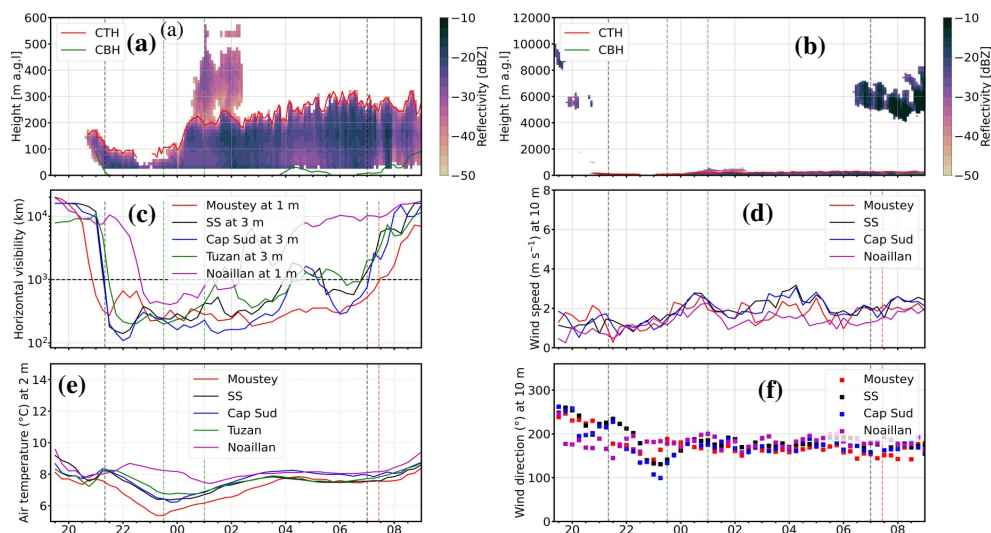
1038 **Figure 6:** As in Figure 4 but for the 5-6 January 2020 (case study 2, IOP6). The red vertical dashed  
 1039 line indicates the sunrise.



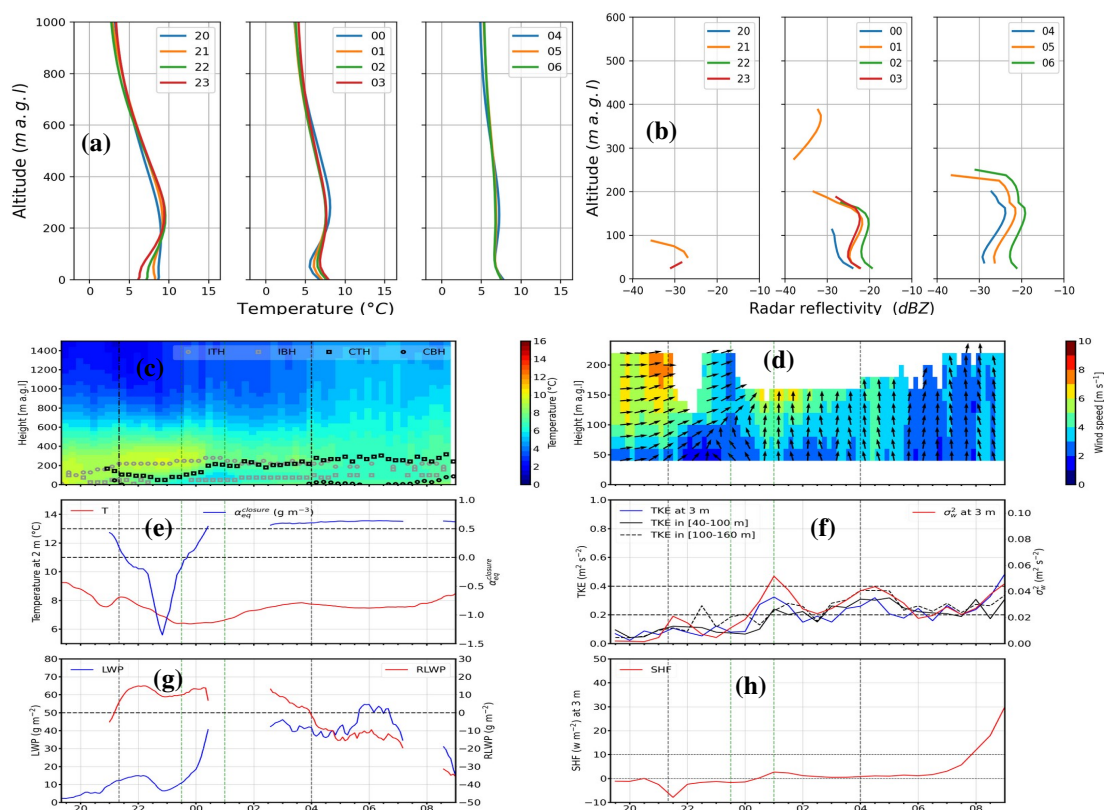
1040 **Figure 7** : As in Figure 3 but for the 8-9 February 2020 (case study 3, IOP 11)



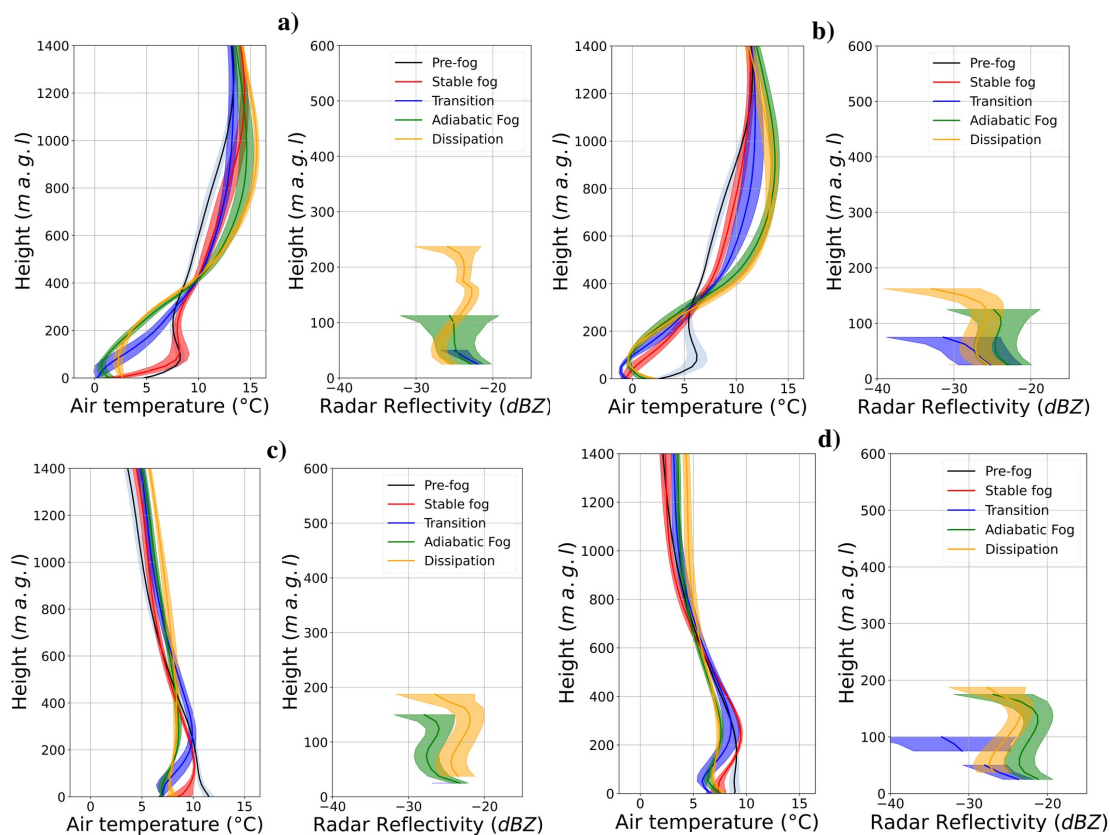
1041 **Figure 8:** As in Figure 4 but for the 8-9 February 2020 (case study 3, IOP 11).



1042 **Figure 9 :** As in Figure 3 but for the 7-8 March 2020 (case study 4, IOP 14).



1043 **Figure 10** : As in Figure 4 but for the 7-8 March 2020 (case study 4, IOP 14). The LWP, RLWP,  
 1044 and  $\alpha_{\text{eq}}^{\text{closure}}$  are disrupted between 00:30 and 02:30 UTC because the LWP estimated by the MWR  
 1045 take into account the liquid water in the advected stratus.



1046 **Figure 11:** Vertical profiles of air temperature and radar reflectivity put together for each fog case study (a) for case 1,  
 1047 (b) case 2, (c) case 3 and (d) case 4. Line and shaded area indicate the mean and standard deviation of air temperature  
 1048 and radar reflectivity during each fog phase.